Utrecht University

NIOZ Royal Netherlands Institute for Sea Research

Ifremer

MASTER'S THESIS

Tidal Dynamics of Capbreton Canyon and Their Influence on Resuspension of Sediment

Author:
Yvo Werner

Supervisors:
Prof. dr. L.R.M. (Leo) Maas
Dr. Henko de Stigter
Dr. Mélanie Diaz
Dr. Ricardo Silva Jacinto

September 8, 2024

Yvo Werner

Tidal Dynamics of Capbreton Canyon and Their Influence on Resuspension of Sediment

Acknowledgements

First and foremost, I wish to express my deepest gratitude towards all of my supervisors. I enjoyed working with every single one of you and couldn't have wished for a better team to guide me through this academically challenging project. I feel honoured by the amount of time that each of you has dedicated to the success of this thesis and am grateful for all of your constant input, guidance, encouragement and inspiration. It has been an absolute pleasure exploring the depths of Capbreton Canyon with all of you, from gathering the data on the ship together with most of you, to diving into the complex physical processes that cause them back on land.

Keeping this thought, I want to first thank Mélanie Diaz and Henko de Stigter for putting their trust in me, and enabling me to go on the research cruise in the first place. Without it, all of this wouldn't have happened for me and I am very grateful that it did. I am also deeply grateful to Henko for his constant support and trust; from arranging a suitable arrangement for regular travel to Texel to giving me the opportunity to help him with the summer course (and for staying supportive even when things didn't go as planned). I would also like to extend my heartfelt thanks to Mélanie for her invaluable input, taking the time to supervise me despite starting a new job and for being such a great and welcoming host on our trip to Brest.

I want to thank Leo Maas for all his unwavering support and guidance; for introducing me to internal waves, helping me interpret the data, pointing me towards new ideas and still leaving me the freedom to explore the data in my own ways and at my own pace. A special thanks also goes out to his wife Cathy for providing a welcome break from the academic discussions with great conversation and a delicious lunch after the supervisor meetings.

I also want to thank Ricardo Silva Jacinto for his great company during the research cruise as part of our two-man CTD night shift, for taking the time to travel to Texel to help me with his expertise and for being a great discussion partner for all matters, academic or not.

Ultimately, I want to also thank the other members of the research cruise, namely Bernard Dennielou, Chris de Blok, Lénaig Brun, Pauline Le Monier, Rose Bieszczad, Shaheen Wahab and Yoann Godfrin for providing many memorable moments from this cruise and many entertaining games of caracol. I would also like to thank the crew of the *RV Pelagia* without whom none of this data could have been collected. Thank you for enabling me to have a great time aboard the ship, from being able to get an engine room tour to having a welcoming bridge willing to answer all the curious questions of a new guy out at sea.

Last but certainly not least, I would like to thank my friends and family for their unwavering support throughout this project. Specifically, I would like to thank my partner Céline for encouraging me to take this opportunity to go on the ship even though it did not fit into our plans at the time at all. I also want to thank her for all her unconditional support, especially during the long days of thin nerves during the writing process and for always being able to lift my spirit nonetheless. Additionally, I would like to thank my parents Marion and Jürgen for supporting my late decision to pursue physical oceanography and for enabling me to finish this degree in the first place.

Abstract

This thesis uses observations to investigate the tidal dynamics and sediment transport processes within Capbreton Canyon, a submarine canyon located in the southeastern Bay of Biscay. Submarine canyons serve as key conduits for sediment movement from the coastal shelf to the deep sea but the exact mechanisms involved are still poorly understood. This study focuses on the interactions between internal waves and the canyon's complex topography which can result in increased levels of internal wave energy close to the seafloor able to cause sediment resuspension.

Observations for this study were collected during the PLUMEFLOC campaign aboard the RV Pelagia covering depths from 500 m to 4000 m. The key variables evaluated include temperature, salinity, current velocity, as well as optical and acoustic backscatter from multiple CTDs, ADCPs and OBSs. These variables are used to investigate the structure of the water column and to identify regions of heightened internal wave energy.

Based on these findings, wavelet analysis revealed highly complex baroclinic conditions with varying tidal frequencies dominating the temperature and current velocity signal at different locations along the thalweg of the canyon. A particular focus was placed on observations from a bottom lander deployed along the thalweg of the canyon at a depth of 2500 m, where highly nonlinear phenomena such as breaking internal waves and bores were observed. Throughout the measurement period, periodic transitions between wave steepening and wave breaking are found with upcanyon propagating bores showing signs of sediment resuspension. However, not all internal tidal bores observed during the study led to sediment resuspension, indicating that further research is necessary to understand the specific conditions and factors that contribute to this phenomenon.

Contents

List of Figures

Introduction

<div style="text-align: right; font-size: 2em;">1</div>

1.1 Research Motivation

Submarine canyons are a ubiquitous feature along continental margins around the world with some estimations placing their overall numbers at more than 9500 (Harris, Macmillan-Lawler, et al., 2014). Due to their location and often deep and incising topography, they play an important role in transferring sediment (de Stigter et al., 2011), organic carbon (Baker et al., 2024), and even pollutants such as micro-plastics (Tubau et al., 2015) and trace metals (Tarrés et al., 2023) from the shallower coastal regions to the deep sea. Their complex and variable topography actively shapes, and is influenced by, the broader oceanographic conditions. It also drives numerous processes such as internal wave breaking (Alberty et al., 2017), deep ocean mixing (Vic et al., 2019) and nutrient upwelling (Woodson, 2018); many of which remain poorly understood.

Capbreton Canyon, located in the southeastern Bay of Biscay, presents a promising location for studying these interactions with the Bay of Biscay being recognised as one of the major generation hotspots for internal tides worldwide (Baines, 1982). Furthermore, the canyon is one of the largest and most geomorphologically complex features in the region, deeply incising both the Aquitaine and Cantabrian continental shelves (Mulder et al., 2012). Its diverse bathymetry extending into depths up to 3500 m and features ranging from gently sloping terraces to steep, vertical canyon walls, make it an ideal site for studying the interactions of internal tides with the canyon's topography.

The effects of such interactions have been observed across the globe (e.g. Li et al., 2019; Aslam et al., 2018; Hall et al., 2017). Internal tides contain substantial amounts of energy with roughly 30% of barotropic tidal energy being transferred to internal tides over deep-ocean ridges alone (Gerkema and Zimmerman, 2008). When internal tides interact with submarine topography such as canyon walls or ridges, a large share of this energy can be focused and dissipated through shoaling and breaking of these internal waves (e.g. Alberty et al., 2017). Furthermore, these interactions are also thought to be responsible for periodic sediment resuspension (van Haren, 2023) and thought to contribute to the formation of nepheloid layers (e.g. Masunaga et al., 2017; Tian et al., 2022) which act as an important pathway for lateral suspended matter transport. While recent studies have started to explore the relationship between internal wave dynamics and sediment resuspension (e.g. Guiastrennec-Faugas et al., 2020), large aspects of the mechanisms involved are still largely unknown, especially in the deeper regions of the canyon.

This research aims to narrow these knowledge gaps by contributing observational evidence from a research cruise, in order to better understand the connection between internal tides and sediment dynamics within Capbreton Canyon. More specifically, this study will focus on identifying regions of enhanced internal wave energy and verifying the presence of internal tides at different locations within the canyon. Additionally, different manifestations of internal wave energy dissipation, most notably shoaling and breaking of internal waves, will be examined as well as their implications for sediment resuspension. The following research questions have helped guide this process:

1. **What are the hydrographic boundary conditions that force the Capbreton Canyon system?**
   This question focuses on the physical properties that modulate internal tides within the canyon such as the barotropic conditions that generate them as well as the stratification profile of the water column that influences their propagation (Barbot et al., 2021). The influence of the water masses and the structure of the water column is topic of Section 4.1.1 while the barotropic conditions within Capbreton Canyon will be discussed in Section 4.1.2.

2. **Where can enhanced internal wave activity and energy dissipation be expected?**
   This question addresses where internal tides might be present within the Capbreton Canyon as well as the spatial variability of their energy. When internal tides encounter a boundary such as the topography of Capbreton Canyon, they are reflected. Under certain conditions, this reflection can lead to focusing of internal wave energy in certain areas of the canyon. Here, enhanced levels of turbulence and mixing might be expected, possibly sufficiently strong enough to cause sediment resuspension as well. The presence of internal tides within Capbreton Canyon is evaluated in Section 4.1.3 while the identification of regions of enhanced internal wave energy is topic of Section 4.1.4.

3. **Which role does internal wave activity play in sediment resuspension observed within the canyon?**
   This question focuses explicitly on the connection between internal tides and sediment resuspension. More specifically, the focus is on turbulent processes such as internal wave breaking that are able to resuspend sediment near the seafloor. Observations of internal wave breaking will be presented in Section 5.1.1. Their connection to sediment resuspension, in this case through the presence of an internal tidal bore, will be discussed in Section 5.1.2.

Before answering these research questions, however, the following sections of this chapter will provide an introduction into the concepts and theories necessary to evaluate and interpret the observations presented in the later chapters. First, they will introduce the fundamentals of internal wave theory (Section 1.2), followed by background information on the research area (Section 1.3). This chapter will be followed by a brief explanation on the data collection during the research cruise (Chapter 2) as well as a chapter on the methodologies applied to answer the research questions (Chapter 3) before introducing the results mentioned above.

1.2 Internal Wave Theory

1.2.1 Linear Wave Theory

Many key characteristics of internal waves can be explained by treating them similarly to the more familiar surface gravity waves. The corresponding theoretic field is called *linear wave theory* and its key aspects relating to this study will be introduced and shortly derived in the next few paragraphs. The underlying assumption of this theory - as the name already suggests - is that nonlinear terms, i.e. products of unknown variables signifying, for example, advection, are neglected. This greatly simplifies the problem but at the same time comes at the cost of sacrificing information on interactions between the waves as each wave is assumed to be independent. This assumption holds true when the wave amplitude is sufficiently 'small', i.e. when the horizontal velocity of the water parcels is much smaller than the phase speed (Gerkema and Zimmerman, 2008). Although, internal waves often show nonlinear characteristics in observations (an example of which will be provided in Chapter 5) many important aspects can already be deduced by neglecting this nonlinearity such as, for example, the overall frequency range in which they occur and the pathways along which their energy propagates. The following paragraphs will derive these key concepts where most of the following approaches and derivations have been taken from either an internal reader by NIOZ (Gerkema and Zimmerman, 2008) or from the lecture notes created by Prof. Maas of Utrecht University in the context of the course *waves in geophysical fluids* (Maas, 2019).

The starting point for these derivations are the fundamental five equations that describe fluid motion in the ocean (Kundu, 1990). Under assumption of the Boussinesq approximation they read:

$$\frac{\partial u}{\partial t} - fv + \tilde{f}w = -\frac{1}{\rho_0}\frac{\partial p'}{\partial x} \tag{1.1a}$$

$$\frac{\partial v}{\partial t} + fu = -\frac{1}{\rho_0}\frac{\partial p'}{\partial y} \tag{1.1b}$$

$$\frac{\partial w}{\partial t} - \tilde{f}u = -\frac{1}{\rho_0}\frac{\partial p'}{\partial z} + b \quad \text{with} \quad b = -\frac{\rho' g}{\rho_0} \tag{1.1c}$$

$$\frac{\partial u}{\partial x} + \frac{\partial v}{\partial y} + \frac{\partial w}{\partial z} = 0 \tag{1.1d}$$

$$\frac{\partial b}{\partial t} + N^2 w = 0 \quad \text{with} \quad N^2 = -\frac{g}{\rho_0}\frac{\partial \overline{\rho}}{\partial z} \tag{1.1e}$$

These equations contain five unknowns: the horizontal velocities u and v, the vertical velocity w, the density ρ and the pressure p where overbars (e.g. $\overline{\rho}(z)$ in 1.1c) indicate mean or background values and primes indicate perturbations (e.g. p' in 1.1b). Additionally, the restoring forces of internal waves are already included, namely the buoyancy b and the planetary vorticity vector decomposed into its radial component f and tangential component $\tilde{f}$. Connected to the buoyancy through equation 1.1e, the Brunt-Väisälä or buoyancy frequency N is also introduced which describes the frequency at which a fluid parcel oscillates around its equilibrium location after having been temporarily displaced under

the assumption that all variables remain constant. Since there are five unknowns and five equations given, this problem is well-defined and a single equation for one of the unknown variables can easily be derived. The choice of which variable to derive the equation for, can be made freely. However, it is common to choose the vertical velocity w, as the boundary conditions that will need to be imposed later on are more easily defined in terms of this variable (Gerkema and Zimmerman, 2008).

Thus, the vertical velocity will also be chosen here and the corresponding equation can be derived as follows. First, $\partial/\partial z$ of equation 1.1b and $\partial/\partial y$ of equation 1.1c is taken and subtracted. Using the continuity equation 1.1d, this yields:

$$\frac{\partial}{\partial t}\left(\frac{\partial w}{\partial y} - \frac{\partial v}{\partial z}\right) = \left(\tilde{f}\frac{\partial}{\partial y} + f\frac{\partial}{\partial z}\right)u + \frac{\partial b}{\partial y} \tag{1.2}$$

Similarly, $\partial/\partial z$ of 1.1a and $\partial/\partial x$ of 1.1c are combined under the same approach:

$$\frac{\partial}{\partial t}\left(\frac{\partial u}{\partial z} - \frac{\partial w}{\partial x}\right) = \left(\tilde{f}\frac{\partial}{\partial y} + f\frac{\partial}{\partial z}\right)v - \frac{\partial b}{\partial x} \tag{1.3}$$

And lastly, $\partial/\partial y$ of 1.1a and $\partial/\partial x$ of 1.1b are combined to:

$$\frac{\partial}{\partial t}\left(\frac{\partial v}{\partial x} - \frac{\partial u}{\partial y}\right) = \left(\tilde{f}\frac{\partial}{\partial y} + f\frac{\partial}{\partial z}\right)w \tag{1.4}$$

Subtracting $\partial^2/\partial y\partial t$ of 1.2 and $\partial^2/\partial x\partial t$ of 1.3 gives:

$$\frac{\partial^2}{\partial t^2}\left(\nabla_H^2 w - \frac{\partial}{\partial z}\left[\frac{\partial u}{\partial x} + \frac{\partial v}{\partial y}\right]\right) + \left(\tilde{f}\frac{\partial}{\partial y} + f\frac{\partial}{\partial z}\right)\frac{\partial}{\partial t}\left(\frac{\partial v}{\partial x} - \frac{\partial u}{\partial y}\right) - \nabla_H^2\frac{\partial b}{\partial t} = 0 \tag{1.5}$$

where ∇_H^2 denotes the horizontal Laplacian operator:

$$\nabla_H^2 \equiv \frac{\partial^2}{\partial x^2} + \frac{\partial^2}{\partial y^2} \tag{1.6}$$

The square bracket can now be rewritten with 1.1d, the Coriolis terms with 1.4 and the last term with 1.1e. This gives:

$$\frac{\partial^2}{\partial t^2}\nabla^2 w + \left(\vec{f}\cdot\nabla\right)^2 w + N^2\nabla_H^2 w = 0 \tag{1.7}$$

with ∇^2 representing the three-dimensional Laplacian operator and $\vec{f} = (0, \tilde{f}, f)$. Since the goal is to describe the fluid motion as a wave, a periodic wave solution is imposed $w \sim e^{-i\omega t}$ and 1.7 can be written as:

$$\left(N^2 - \omega^2 + \tilde{f}^2\right)\frac{\partial^2 w}{\partial y^2} + 2f\tilde{f}\frac{\partial^2 w}{\partial y\,\partial z} + \left(f^2 - \omega^2\right)\frac{\partial^2 w}{\partial z^2} + \left(N^2 - \omega^2\right)\frac{\partial^2 w}{\partial x^2} = 0 \tag{1.8}$$

where x denotes the east-west direction and y the north-south direction.

In this equation, each second-order derivative has a different coefficient. Thus, waves propagating in the x-direction show different behaviour than those propagating in the y- and z-direction. To simplify the behaviour in the horizontal, i.e. in order to get rid of

this anisotropy, the traditional approximation can be applied which would see those terms dropped where $\tilde{f}$ is involved. In essence, it simplifies the treatment of the Coriolis force by neglecting the components that act both vertically and horizontally on the vertical flow. This is valid when the horizontal motions are much larger than vertical motions, which is often the case in large-scale geophysical flows. However, under weak stratifications (where vertical motion is easily initiated) and in mid-latitudes (where $\tilde{f} \approx f$), these 'non-traditional' effects can still be significant (Gerkema and Zimmerman, 2008). As the aim of this section is to introduce the key characteristics of internal waves and since they can be derived more readily under this assumption, the traditional approximation will be applied. However, it is worth noting that Capbreton Canyon extends to great depths where stratification can be expected to be weak and is also located in the mid-latitudes, so non-traditional effects may be significant in this case.

With the use of the traditional approximation, the terms containing $\tilde{f}$ vanish and equation 1.8 is simplified. The result is the desired equation for the vertical velocity w and it reads:

$$\left(N^2 - \omega^2\right) \nabla_H^2 w - \left(\omega^2 - f^2\right) \frac{\partial^2 w}{\partial z^2} = 0 \tag{1.9}$$

From this equation, two important concepts for this study can be derived: (1) the *dispersion relation* for internal wave and (2) their *characteristic coordinates*.

The dispersion relation is derived when a 2D wave-like solution is imposed on equation 1.9. As there is no longer anisotropy present in the horizontal direction, a wave propagating in the x-direction can be arbitrarily chosen knowing that any results also apply to the y-direction. Thus, the wave in x-direction ($\partial/\partial y = 0$) is described by:

$$\left(N^2 - \omega^2\right) \frac{\partial^2 w}{\partial x^2} - \left(\omega^2 - f^2\right) \frac{\partial^2 w}{\partial z^2} = 0 \tag{1.10}$$

and its solution shall be described by:

$$w = e^{i(kx + mz)} \tag{1.11}$$

where k and m describe the wave number in the x- and z-direction, respectively. They can be combined to the wave vector $\vec{k} = (k, m) = \kappa(\cos\theta, \sin\theta)$ with the wave vector magnitude $\kappa = \sqrt{k^2 + m^2}$. Using the polar notation of the wave vector and plugging it into equation 1.10 gives

$$\omega^2 = N^2 \cos^2\theta + f^2 \sin^2\theta \tag{1.12}$$

which is known as the **dispersion relation**.

The dispersion relation is one of the essential equations of internal wave theory and at its core shows how the two restoring forces, the buoyancy and the Coriolis force, relate to the frequency of the internal wave. It also highlights interesting characteristics of internal waves.

For one, while ω is dependent on the direction of the wave vector $\vec{k}$, it is independent from its magnitude. As will be shown below, this implies that the group velocity

$$\vec{c}_g = \left(\frac{\partial\omega}{\partial k}, \frac{\partial\omega}{\partial m}\right) = \frac{(N^2 - f^2)\cos\theta\sin\theta}{\kappa\omega}\left(\sin\theta, -\cos\theta\right) \tag{1.13}$$

is perpendicular to $\vec{k}$. Using the trigonometric identity $\cos^2 \theta + \sin^2 \theta = 1$ and applying it to ω, so that $\omega^2 = \omega^2(\cos^2 \theta + \sin^2 \theta)$, the group velocity can be rewritten as:

$$\cot^2 \theta = \frac{\omega^2 - f^2}{N^2 - \omega^2} \tag{1.14}$$

Another important conclusion can be drawn from this equation. Since the right hand side must be positive, the internal wave frequency must lie within an interval bordered by f and N. Depending on whether $|f| > N$ or $N < |f|$, the corresponding frequency intervals are:

$$\boxed{(I) \quad N \leq \omega \leq |f| \quad \text{or} \quad (II) \quad |f| \leq \omega \leq N} \tag{1.15}$$

Consequently, the dispersion relation is a fundamental relationship in observing and studying internal waves. It not only provides insight into the interesting aspects of how internal waves behave but in the scope of this work has also informed us where and how to identify them in the data. The frequency bands of 1.15 give valuable information on where internal waves might be expected and which scales or frequencies should be used, for example, in wavelet analysis. Additionally, it shows that the internal wave frequency ω is determined by the angle of propagation θ and vice versa. This implies that for a set internal wave frequency, for example the internal tide at M2 frequency, the angle of propagation with the vertical remains unchanged. This is especially remarkable when considering interactions of internal waves with boundaries such as the sloping thalweg of Capbreton Canyon or its side walls. Even after reflection, the angle of the internal wave must remain unchanged with regard to the vertical, a characteristic in strong contrast to what is 'usually' known in the context of reflection where the angle with respect to the normal to the reflecting surface remains unchanged.

The rewritten form of equation 1.14 also provides information on the trajectories of internal wave energy. The direction in which internal wave energy propagates is given by the direction of the group velocity $\vec{c_g}$ which was described in equation 1.13. If we define $\mu_\pm = \pm \cot \theta$, it becomes apparent that equation 1.14 also contains information on the slopes $\mu_\pm$ of the internal wave energy which are also known as the **characteristic coordinates**. The corresponding equation to $\mu_\pm$ is given by the square root of equation 1.14:

$$\boxed{\mu_\pm = \pm \left(\frac{\omega^2 - f^2}{N^2 - \omega^2} \right)^{1/2}} \tag{1.16}$$

The information of the pathways along which internal wave energy travels can then be used to identify regions within Capbreton Canyon where internal wave energy is focused; regions that have been shown to have increased levels of turbulence near the seafloor (Aslam et al., 2018).

In general, tidal energy is focused and trapped in submarine canyons due to the interaction of these rays of internal wave energy with the bottom slope or the sidewalls of the canyon. The key variable that describes this process is the ratio of the slope of the seafloor s_b relative to the slope of the internal wave beam, also known as the **wave steepness parameter** α

(Cacchione et al., 2002). The slope of the internal wave beam is given by that of its characteristic coordinates, so α can be defined as:

$$\alpha = \frac{s_b}{\mu_\pm} = \frac{s_b}{((\omega^2 - f^2)/(N^2 - \omega^2))^{1/2}} \qquad (1.17)$$

where:

- s_b is the local slope of the seabed.
- $\mu_\pm$ are the characteristic coordinates determining the slope of the internal wave beam.
- ω is the internal wave frequency.
- f is the Coriolis frequency dependent on latitude φ with $f = \sin \varphi$.
- N is the buoyancy frequency.

Based on the value of α, three distinct reflection regimes can be identified. Note that the flat-bottom case ($\alpha = 0$) has been omitted in this listing, so that only cases found within this canyon setting will be introduced. The remaining regimes are:

1. **Supercritical Regime ($\alpha > 1$):**
   - The slope of the seafloor is steeper than the internal wave slope. This results in a reflection of the internal wave backward, opposite to its original horizontal direction while maintaining its downward propagation component. In this context, this means that steep canyon walls can reflect an internal wave deeper into the canyon towards the seafloor causing internal wave energy to be concentrated near the bottom. In the case of a supercritical thalweg slope, this causes an internal wave approaching from deeper waters to be reflected towards the open ocean again. In the horizontal, this interaction often results in standing wave-like patterns as the reflected waves interact with the incoming waves (Alberty et al., 2017).

2. **Subcritical Regime ($\alpha < 1$):**
   - In this case, the seafloor is gentler than the internal wave slope and the wave continues to propagate into the same horizontal direction after its reflection while changing its vertical propagation component from downward to upward. In a canyon setting, this results in internal wave energy being focused further into the canyon in the case of internal waves approaching from the open ocean.

3. **Critical Regime ($\alpha = 1$):**

- When the seafloor slope matches that of the internal wave beam, the reflection becomes critical. The result is strong focusing of internal wave energy at the seafloor, often connected to dissipation of internal wave energy via internal wave breaking. Numerical models have shown that in areas with near-critical bottom slopes, bottom velocities are enhanced and that they are hotspots for internal wave breaking and high levels of turbulence (Aslam et al., 2018).

With the help of these regimes, it is then possible to explain how submarine canyons are able to trap and focus internal wave energy. The side walls of canyons are typically steep and can be considered to be supercritical which focuses internal wave energy towards the seafloor. Depending on the slope of the bottom of the canyon, the focused energy is then either reflected back into the open ocean or directed further into the canyon where subsequent focusing can ultimately lead to energy dissipation via internal wave breaking. This focusing of internal wave energy via the subcritical regime has important implications for the ability of internal waves to resuspend sediment. Geological data indicates that these regions, where a transition from the subcritical to the critical regime is present, show enhanced sediment transport, particularly in the up-canyon direction. More specifically, this process is hypothesised to be caused by internal tidal bores — the equivalent of the 'run-up' of waves on the beach after they have broken — that are associated with high bottom velocities and high amounts of turbulence (Amaro et al., 2016).

1.2.2 Nonlinear Wave Theory

The previous section has shown that many aspects of internal waves can be explained by neglecting nonlinear effects, especially in the context of small wave amplitudes. This section will now introduce the key concepts of internal wave theory that are applicable when this assumption no longer holds true. An example of this would be nonlinear steepening of a wave due to interactions with its surrounding topography similar to waves shoaling on a sandbar. In the application of this study, this means that due to the complex topography of Capbreton Canyon (see Section 1.3), the effects of nonlinearity will have to be included in order to understand the internal waves observed there. For this section, the focus will be placed on the effects of nonlinearity on a single wave propagating horizontally along an isopycnal, also known as an internal solitary wave (ISW). A key characteristic ISWs is their permanence of form, meaning that it does not change its shape as it propagates.

In its most basic sense, a nonlinear wave can be described by the following equation (Gerkema and Zimmerman, 2008):

$$\frac{\partial \eta}{\partial t} + \frac{\partial \eta}{\partial x} + \epsilon \eta \frac{\partial \eta}{\partial x} = 0 \qquad (1.18)$$

where the field $\eta(x,t)$ describes the amplitude of the wave at location x and time t, and parameter ϵ describes a certain amount of nonlinearity. The first term and second term in this equation depict the temporal and spatial evolution of the shape of the wave. The third term, then, describes the nonlinear interaction of strength ϵ between the amplitude of the wave η as well as the spatial evolution of its amplitude $\partial \eta / \partial x$.

A fundamental insight into the effects of nonlinearity can be gained when looking at a general solution to this equation. With referral to Gerkema and Zimmerman (2008) for details, this general solution can be described by function $F(\xi)$, where $\xi = x - (1 + \epsilon\eta(x,t))t$. Here, ξ acts as a coordinate frame that moves along with the wave. The speed at which this coordinate frame, and thus also the wave, is moving, is given by the coefficient $(1 + \epsilon\eta(x,t))$. This immediately conveys that nonlinear waves must have an amplitude-dependent wave speed. Since the nonlinearity factor ϵ remains constant, the wave speed is only influenced by the amplitude of the wave $\eta(x,t)$. For observations of nonlinear internal waves, this means that larger internal waves will arrive first, followed by ever smaller amplitude waves. Furthermore, this implies that the wave crest move faster than the wave troughs which can lead the crests to overtake the troughs, resulting in wave breaking.

What this equation is not immediately able to explain, is how internal solitary waves are able to retain their shape over long distances. To solve this, equation 1.18 will need to be modified to include the forces acting on the wave when it steepens as it propagates. A common equation that is used in the research of ISWs that includes these forces is the Korteweg-de Vries (KdV) equation (Korteweg and de Vries, 1895). Although it has been found to be only applicable for weak-nonlinearity and small wave amplitudes, it still is able to explain this fundamental feature of ISWs. In accordance with the notation chosen by Boegman and Stastna (2019), where a subscript denotes partial differentiation, it can be written as:

$$A_t + cA_x + \alpha AA_x + \beta A_{xxx} = 0 \qquad (1.19)$$

where:

- A represents the amplitude of the wave.
- c is the linear phase speed of the wave.
- α is the nonlinearity coefficient.
- β is the dispersion coefficient.

The equation captures the two opposing forces acting on the wave: steepening due to nonlinearity and spreading due to dispersion. It is the balance of both forces that enables the ISW to maintain its form over long distances. Without this balance, the wave will either steepen and break due to the stronger influence of nonlinear effects or dissolve into its individual frequencies due to dispersion. In other words, the nonlinear effects drive energy towards the short scale while the dispersive effects cause it to spread out.

1.2.3 Internal Wave Generation & Dissipation

This section describes the processes that cause the generation and dissipation of internal waves. Both involve an interaction of topography with either external processes (e.g. the tide) or with the internal waves themselves which is why they will be covered in the same section. First, the generation of internal waves, more specifically of internal tides, will be discussed where also their intermittent nature will be explained; another important observational characteristic of internal waves used in this study. Lastly, the mechanisms involved in the dissipation of internal wave energy will be discussed where wave-topography
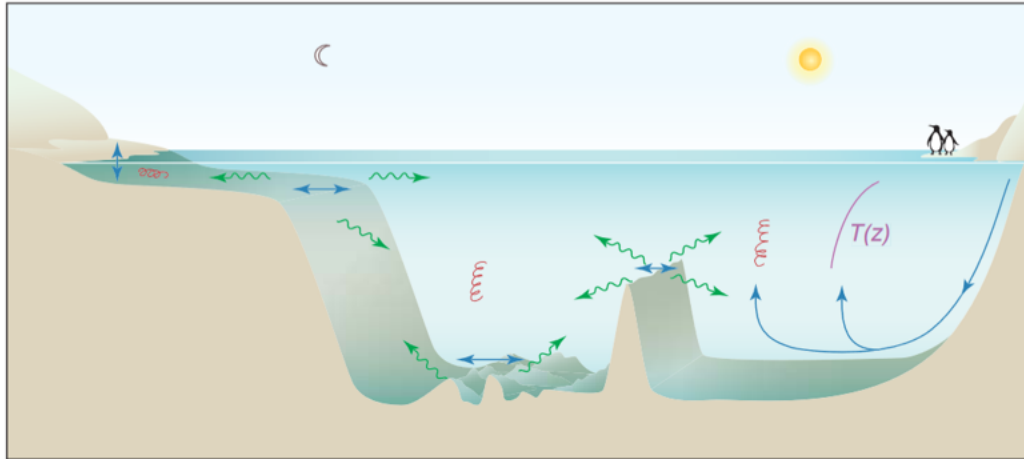
Fig. 1.1: Generation sites of internal tides (green arrows) through interactions of topography with the barotropic tidal current at the edge of the continental shelf or with features of the deep ocean. T(z) denotes the temperature profile as a function of depth. Taken from Garrett (2003).

interactions are able to cause shoaling and breaking similar to the case of surface waves on a beach.

The typical idea of tides is usually that of the barotropic tide typified by the periodic motion of the ocean caused by the gravitational pull of the Moon and Sun. Due to their large wavelength, barotropic tides propagate in the oceans as shallow water waves and their rising and falling is observed throughout the entire water column. The tidal currents that arise as a result are predominantly horizontal. However, when they encounter an obstacle (e.g. the continental shelf) they are diverted upwards inducing a vertical component that periodically lifts isopycnals up and down. Due to the generally stratified nature of the ocean, this vertical displacement induces an oscillation proportional to the strength of the local stratification as water parcels are lifted out of their equilibrium position. This oscillation of isopycnals is able to propagate long distances and has been introduced in Section 1.2.1 as an internal wave. Since the extent of the vertical displacement is directly bound to the frequency of the tide, the resulting wave will also possess a tidal frequency which is why these internal waves are called **internal tides**. An overview of the locations where internal tides are generated can be found in Figure 1.1.

While the generation of internal tides might seem conceptually straight forward, its manifestations in reality are highly complex and it is easy to understand why.
First, of course, the topography with which the tidal current interacts is highly complex itself. While continental slopes or submarine canyons are often approximated by flat bottoms or other simple two-dimensional shapes, their actual topography is diverse and complex. Observations of a local internal wave environment are further complicated by the sheer amount of topographic features that are able to interact with the tide. Measurements will include internal waves generated locally but also those generated up to thousands of kilometres away (e.g. Marques et al., 2021). Since the main driver of their generation are barotropic tidal currents, local currents or even larger scale oceanographic currents are also able to interfere (Dauhajre et al., 2023). Additionally, the strength of the stratification along

the path in front of an internal wave also influences its propagation (Barbot et al., 2021). Due to these ever changing conditions under which they are generated and under which they propagate, internal waves have an inherently **intermittent nature** (Wunsch, 1975). While this complicates their observations, it also makes them more easily distinguishable from the barotropic tides as these do not show this intermittency. Therefore, this characteristic was also included in the evaluation of velocity and temperature profiles in this study (see Section 4.1.3).

Having established the general working principle of how internal tides are generated, the focus can now be shifted to how their energy is dissipated. Section 1.2.1 has already introduced the pathways along which internal wave energy propagates containing both a horizontal as well as a vertical component. Unlike surface waves, which exclusively propagate horizontally, this vertical component enables internal wave energy to propagate and ultimately dissipate in different depths to where it was generated. This has important implications for the energy transfer between the shallower regions of the oceans, where most internal wave energy is generated (Gerkema and Zimmerman, 2008), and the deeper regions where the energy might be focused and dissipated through internal wave breaking. Understanding this mechanism is crucial, as internal wave breaking influences a variety of processes on and near the seafloor as well as in the water column above. For example, internal wave breaking on continental slopes has been found to trigger sediment resuspension due to enhanced turbulence levels (Boegman and Stastna, 2019). Furthermore, its associated sediment transport in the up- and downslope direction shapes the seafloor and possibly even that of the entire continental slope (Cacchione et al., 2002; Puig et al., 2004). These enhanced levels of turbulence also cause significant diapycnal mixing as fluid parcels from deeper regions are transported into higher reaches of the water column and redistributed by chaotic advection (La Forgia, Cavaliere, et al., 2021), sometimes also causing increases in biological productivity (Woodson, 2018). This deep-ocean mixing caused by internal wave breaking has even been postulated as the missing link in closing the abyssal circulation (Mashayek et al., 2017).

The general principle of internal wave breaking is very similar to that of surface waves (see Figure 1.2). As the wave approaches a sloping boundary it starts to shoal leading to steepening of the trailing edge of the wave causing it to transition from a symmetric wave form to an asymmetric wave form. This shoaling causes wave energy to be further focused towards the seafloor and is able to cause strong near-bottom current velocities (Boegman and Stastna, 2019). Once a critical threshold is reached, the steep back of the wave becomes unstable and the wave starts to break.
Many different forms of internal wave breaking have been described in the literature. In this study, a classification introduced by Boegman, Ivey, et al. (2005) is used which introduces three types of internal wave breaking: (1) plunging breakers, (2) collapsing breakers, and (3) surging breakers.
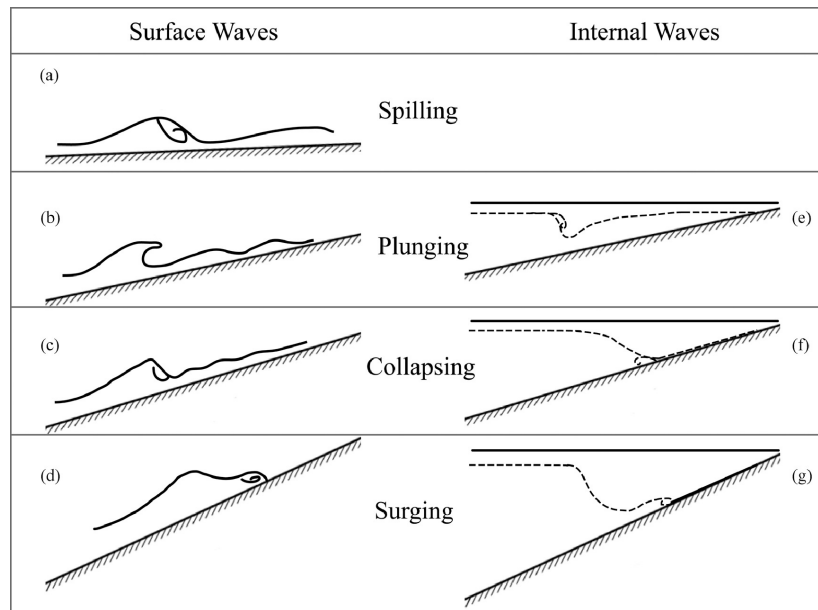
Fig. 1.2: Schematic representation of the different breaker types divided into their surface wave manifestations (a–d) and internal wave manifestations (e–g). The dashed line depicts the pycnocline and the solid line depicts the free surface. Taken from La Forgia, Adduce, et al. (2018).

Expanding on this work, La Forgia, Adduce, et al. (2018) identified the presence of intermediate forms (e.g. the plunging-collapsing breaker) and further specified each of the breaker types as follows:

1. **Plunging Breakers**

   - This breaker mechanism is characterised by strong steepening of the back of the wave followed by a large clockwise overturning circulation in the onshore direction. Due to its high energy content, it is able to induce strong local mixing.

2. **Collapsing Breakers**

   - Here, trapped, dense fluid is sucked downwards towards an adverse pressure gradient region in the bottom boundary layer which causes separation and the formation of a turbulent bolus. This is followed by a partial reflection of the incident internal wave and the generation of a gravity current that rapidly propagates upslope until hydrostatic conditions are reestablished (La Forgia, Tokyay, et al., 2020). Both internal wave energy focusing and increasing levels of asymmetry are able to enhance the adverse pressure gradient (Boegman and Stastna, 2019).

3. **Surging Breakers**

   - This type of breaker is characterised by the absence of instabilities during the shoaling process until the trough of the wave reaches the seafloor. Then, the incident wave is almost reflected and causes the generation of a gravity current of denser water moving upslope.

1.3 Study Area

The Bay of Biscay is a deep basin with water depths up to 5000 m bordered by the European continent to the east and south and otherwise open to the Atlantic Ocean to the west (see Figure 1.3). Four continental margins fringe the Bay of Biscay: the Celtic and Armorican margin to the north, the Aquitaine margin to the east and the North-Iberian margin to the south. The Celtic, Armorican and North-Iberian margins can be classified as "canyon-dominated" while the Aquitaine margin - where the study area is located - can be classified as "tectonic-dominated" (Bourillet et al., 2006). Furthermore, the Aquitaine margin features a submarine plateau near its southern end, the Landes Plateau, that gently dips westward. At the southern side of this plateau, and consequently in the very southeastern corner of the Bay of Biscay is the location of Capbreton Canyon (red box in Figure 1.3). It begins just off the coastal town of Capbreton in France and follows the northern coast of Spain for approximately 300km along a complex, meandering course, before merging with the Cap-Ferret-Capbreton deep-sea fan system at the base of the continental slope at roughly 3500 m depth (Cirac et al., 2001; Gaudin et al., 2006).

Capbreton Canyon started to form during the Middle Eocene, 50 to 40 million years ago, in a subsidence zone where the convergence of the Iberian and European plates caused structural weaknesses (Deregnaucourt and Boillot, 1982). Until the Middle Miocene, 16 to 12 million years ago, the canyon was dominated by depositional processes such as mass flow deposits or overbank sedimentation which caused the canyon to be filled and its morphology to be smoothed (Guiastrennec-Faugas et al., 2020). Since then, the canyon
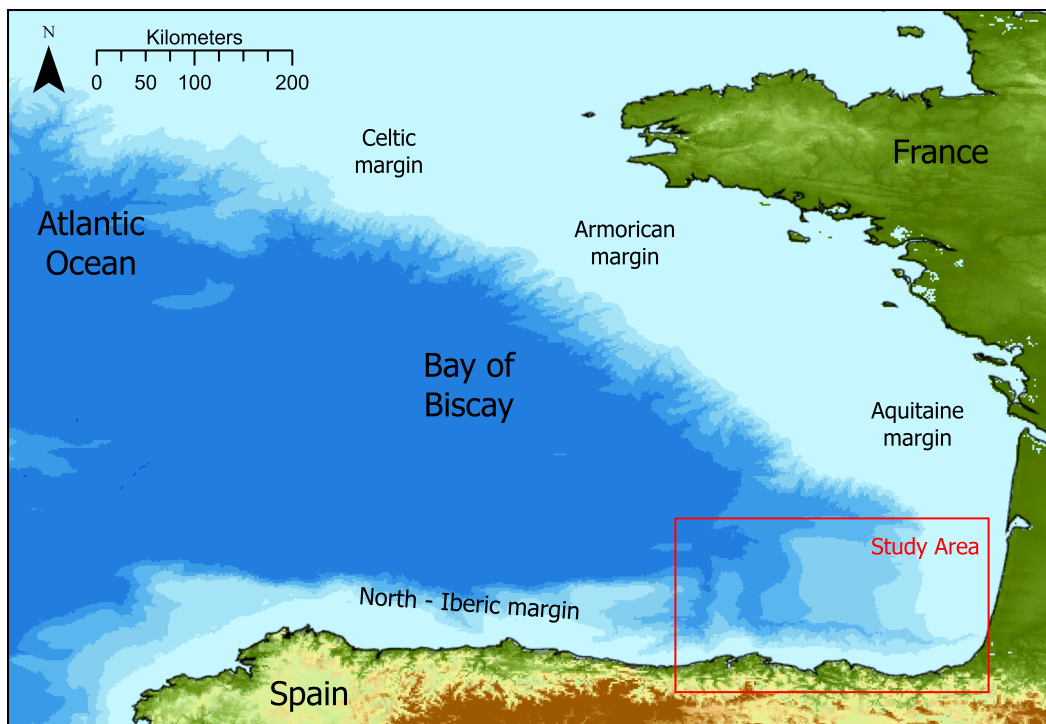
Fig. 1.3: Geographic context of the Bay of Biscay including its bordering continental shelves and the study area (red box). Data provided by GEBCO Compilation Group (2024)

has been dominated by erosional processes, further incising the continental shelf and slope (Ferrer et al., 2008). Due to its connection to the Adour river which enters the Bay of Biscay not far from the canyon's head, Capbreton Canyon can be categorised as a Type 1 canyon (river-associated and shelf-incising) according to the classification system proposed by Harris and Whiteway (2011). This puts it into the same category as the well-known Monterey Canyon (Greene et al., 2002) or the highly-dynamic Congo Canyon (e.g. Shepard and Emery, 1973).

Within the Bay of Biscay, Capbreton Canyon distinguishes itself from other canyons within the region, such as the Whittard, Blackmud or Audierne Canyon, by its complex meandering course (Cirac et al., 2001). Its head is located only in 30 m water depth and forms a deep and wide amphitheatre facing the sea (Gaudin et al., 2006). The overall cross-sectional shape of the canyon is that of a "V", with terraces on both sides along the flanks at tens to hundreds of metres height above the canyon thalweg(Mulder et al., 2012). In the upper part of the canyon, up to about W1°50, this shape is symmetrical but becomes asymmetric further west as the southern flank becomes much higher than the northern flank (Gaudin et al., 2006). The thalweg – the deepest part of the canyon – is generally characterised by a gentle and regular slope in along-axis direction of, on average, 0.8 degrees with the exception of steeper sections at the head of the canyon where slope values can reach up to 7 degrees (Mulder et al., 2012). In the upper reaches of the canyon, the thalweg is narrow with widths in the order of tens of meters. As the canyon widens with depth, the thalweg broadens as well reaching widths of multiple hundreds of meters (Mulder et al., 2012).

Considering the shape of the canyon, it is not surprising that Capbreton Canyon, much like other coastal submarine canyons, acts as a natural conduit for continental and shelf sediments to the deep sea (Guiastrennec-Faugas et al., 2020). This is facilitated by the occurrence of strong alongshore currents that are caused by large NW-SE swells hitting the coast at an oblique angle, and are able to transport large quantities of sediment to the head of the canyon. A study by Idier et al. (2013) tried to quantify this phenomenon and has found that along the Aquitaine coast between 38,000 and 657,000 m^3 of sediment are transport annually. Around the head of the canyon, however, this figure reduces from 40,000 m^3 per year north of the canyon to only 1,000 m^3 per year south of the canyon (Abadie et al., 2006). Not only does this cause significant coastal erosion south of the canyon but it also highlights the large amounts of sediment, predominantly in the fine sand and mud fraction, that are trapped in the head of the canyon and are discharged towards the deeper regions (Mazières et al., 2014).
Another important factor is the input of river sediment through the Adour river which is a major drainage pathway of the Pyrenees Mountains. Throughout history, the river has been repeatedly connected and disconnected from the canyon due to natural and anthropogenic causes and is currently located roughly 15 km south of the canyon head (Klingebiel and Legigan, 1978). Nonetheless, the river is still able to supply sediment indirectly (Brocheray et al., 2014; Mazières et al., 2014) and a study by Petus et al. (2010) has even shown that the river plume is able to reach the head of the canyon 20% of the time due to northward deflection caused by easterly winds.

Once confined by the canyon, this sediment is mainly transported by turbidity currents that can be caused by river floods (Baker et al., 2024), storms (Normandeau et al., 2020), earthquakes (Arai et al., 2013) or even anthropogenic activities like bottom trawling (Payo-Payo et al., 2017). Within Capbreton canyon, additional significant contributions by internal tides and near-inertial internal waves have also been found which, interestingly, are able to transport sediment both up and down the canyon due to their oscillatory nature. (Guiastrennec-Faugas et al., 2020; Mulder et al., 2012).

Data

<div align="right">2</div>

This chapter provides information on how and where the observations at the core of this study were collected. First, Section 2.1 will briefly introduce the research cruise and the main instruments that were used. This is followed by Section 2.2, where the setup of each of the instruments is described and details on their measurement configurations are given.

2.1 Research Cruise

The data for this study were collected during the PLUMEFLOC campaign on board the *RV Pelagia* between September 5 and September 25, 2023. The research cruise was led by NIOZ and started on Terceira, Portugal and ended on Texel, The Netherlands (Figure 2.1a). Within the research area (red rectangle in Figure 2.1a), eight research sites were selected based on their position along the axis of Capbreton Canyon in order to achieve a coherent picture of the depths between 500 m and 4000 m.

The main variables used to investigate the internal tidal dynamics of Capbreton Canyon and to identify their connection to sediment resuspension, consist of temperature, salinity, pressure, current velocity, as well as optical and acoustic backscatter. Their observations were obtained through: (1) conductivity-temperature-depth sensors (CTDs), (2) acoustic Doppler current profilers (ADCPs), and (3) optical backscatter sensors (OBSs). In order to be able to compare measurements of similar properties a combination of these sensors was put at similar measurement locations to ensure complimentary data. The following sections provide further details on each of these sensors as they are deployed on the CTD frame (Section 2.2.1), the moorings (Section 2.2.2) and the bottom lander (Section 2.2.3).
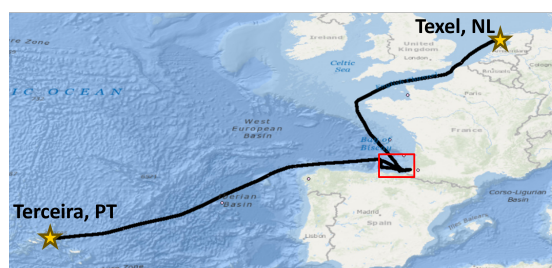
(a) Route of the research cruise

(b) RV Pelagia, ©NIOZ

Fig. 2.1: Route of the RV Pelagia during the PLUMEFLOC campaign (left) and a picture of the ship (right). The red rectangle in the left panel indicates the research area. The cruise started on September 5, 2023 on Terceira, Portugal and ended on September 25, 2023 in Texel, The Netherlands.

2.2 Research Setup

2.2.1 CTD-Rosette System

The CTD-Rosette system consisted of a Seabird 911+ with mounted sensors for pressure, temperature, conductivity, oxygen, fluorescence, photosynthetically active radiation, and light transmission. From these measurements derived parameters included salinity, potential temperature, density, water depth and sound velocity. Furthermore, water samples were taken via the remote-controlled rosette system using 24 PRISTINE ultra-clean sampler bottles developed by NIOZ (Rijkenberg et al., 2015) with a volume of 12 litres each. Samples were taken near the seabed during all casts as well as at 250 m and 500 m above the bottom during the yo-yo operation. From each bottle, two five-litre samples were collected, filtered on board and the residue weighted after the cruise to quantify the amount of suspended particulate matter.

The measurement setup on the frame of the CTD-Rosette system consisted of a downward-facing boxcorer camera, multiple OBSs, an upward-looking ADCP, a particle camera (PAR-TICAM, Gillard et al. (2022)) and, due to depth limitations, at the shallowest research also of a particle sizer (LISST-200X). A picture of the layout (excluding the PARTICAM and LISST-200X) can be seen in Figure 2.2a. During operation, the frame was launched via the mid-ship A-frame winch and was connected via a Kevlar fibre optic cable capable of deep-sea applications. This enabled a real-time view of the gathered data as well as the video feed from the camera located at the bottom of the frame.

Overall, two modes of CTD operation could be distinguished: (1) single cast operation and (2) yo-yo operation. The single cast operation consisted of a single lowering of the frame from the surface to the seafloor (up to roughly 10 m above bottom) and a subsequent raising all the way back to the surface. This was done for all research sites except at 500m where only a yo-yo cast was performed. These casts served the purpose of establishing a first picture of the hydrographic conditions present in the research area and informed the decision on where the moorings and the bottom lander would best be deployed. A transect of single casts crossing the canyon thalweg at research sites 6 and 8 was also planned but had to be discontinued due to bad weather conditions. The yo-yo operation consisted of the periodic lowering and raising of the CTD frame between approximately 10 m above the bottom and 500 m above the bottom with 5-minute stops at three distinct levels: (1) bottom, (2) 250 m and (3) 500 m above bottom. In total, each yo-yo-cast covered at least a time period of 13 h to ensure that a principal semidiurnal tidal cycle ($\approx$ 12.42 h) was fully covered by the observations.

ADCP measurements on the CTD frame were realised with an upward-facing Nortek Aquadopp 2 MHz current profiler attached to the top of the frame. The instrument's measurement configuration consisted of 20 cells, each with a vertical resolution of 50 cm, and a blanking distance of 50 cm above the transducer head. Data was collected at intervals of 60 s, with each measurement being averaged over 30 s. Thus, the first measurement corresponds to a vertical distance of 1 m above the transducer head (blanking distance +

(a) CTD-Rosette system, ©Yvo Werner

(b) Bottom lander, ©Yvo Werner

Fig. 2.2: Photos of the CTD-Rosette system (left) and the bottom lander (right). Pictures taken pre-deployment. Note that in the left panel the PARTICAM and the LISST-200X are not attached.

1 cell size) while the last measurement corresponds to a vertical distance of 10.5 m. The output of the instrument includes current velocity in the eastward, northward and upward direction as well as acoustic backscatter in unitless counts and pressure in decibar.

Lastly, several JFE Advantech optical backscatter sensors were mounted on the CTD-Rosette system as well as along the Kevlar cable. Capable of withstanding water depths up to 6000m, the sensors provided measurements of the turbidity of the water at a frequency of 1 Hz by evaluating the backscattered signal of a 880 nm light source. Their output consisted of turbidity values in the range of 0 - 1000 Formazine Turbidity Units (FTU) as well as temperature in degrees Celsius. The locations of the OBS were chosen so that their readings overlapped with the measurements of other instruments, namely that of the high-frequency Nortek Aquadopp ADCP, so that acoustic and optical backscatter could readily be compared with each other. Thus, one OBS was mounted at the base of the CTD frame, three OBSs were positioned at 1 m, 3 m and 5 m above the Nortek Aquadopp and, water depth permitting, two additional OBSs were positioned at 500 m and 1000 m above the frame on the Kevlar cable in order to gain more information on the water column.

2.2.2 Moorings

Three moorings were deployed in water depths of 500 m, 1000 m and 1500 m along the thalweg of the canyon (positions labelled "M" in Figure 2.3). The overall layout of the moorings consisted of an anchor weight, two IXSEA OCEANO 2500 S universal acoustic releases, a 50 m Dyneema cable, tring of 7 benthos floats, a frame with 3 additional benthos floats carrying a flashlight, satellite beacon and a pickup line with at the end another benthos float.
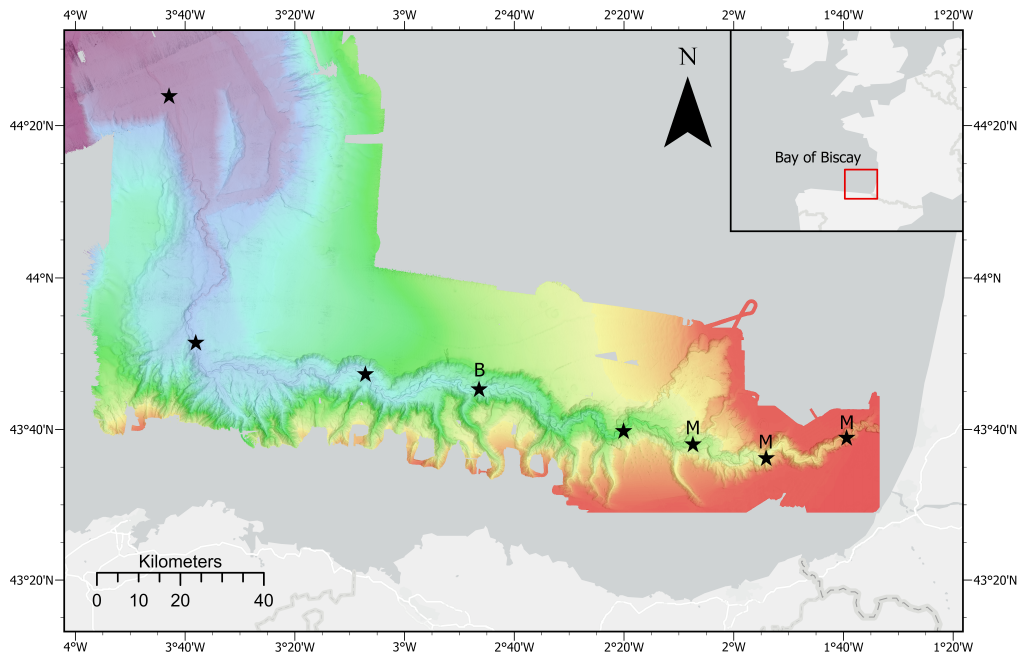
Fig. 2.3: Bathymetric map of the research area based on data provided by Ifremer (see Section 2.3). Stars indicate the research sites while letters denoted the positions of moored deployments ("M" = mooring, "B" = bottom lander).

The measurement assembly near the bottom at approximately 1 meter above bottom (mab) consisted of a sediment trap, a JFE Advantech OBS sensor and an upward facing Nortek 2 MHz Aquadopp current profiler. Similar to the setup on the CTD frame, the Nortek Aquadopp measured in 20 cells with a size 50 cm each and a blanking distance of 50 cm, resulting in measurements available between 1 m and 10.5 m above the transducer head. A notable difference to the setup on the CTD frame is a measurement interval of 120 s and an averaging window of 30 s in this case. On the deepest mooring at 1500 m, a Seabird SBE 37 Microcat CTD was also deployed, providing additional observations of temperature, salinity and pressure every 6 seconds. Along the mooring line, two additional JFE Advantech OBS sensors were mounted; one within the field of view of the Aquadopp at 4 m above the seabed and another at the top of the line at 50 m above the seabed. All OBS sensors were set up to measure every 120 s with a burst of 10 measurements at 1 Hz.

2.2.3 Bottom Lander

The bottom lander, designed by NIOZ (van Weering et al., 2000), was deployed at 2500 m water depth as indicated by the label "B" in Figure 2.3. It measured current velocity, temperature, salinity as well as optical and acoustic backscatter. Its structure consists of a frame of roughly 4 m height with three legs (see Figure 2.2b), each held down to the seabed by three 100 kg iron weights which were released by means of a centrally mounted set of two IXSEA OCEANO 2500 S-Universal acoustic releases.

Current velocity and acoustic backscatter were measured with three ADCPs: a 2 MHz Nortek Aquadopp, and two RDI Workhorse instruments with 1200 kHz and 300 kHz. The 300 kHz RDI Workhorse was mounted on the top of the frame at approximately 4 mab facing upwards and recorded in 109 cells of 1 m every 120 s. It had a blanking distance of 2.2 m and thus provided measurements of the water column between 3.2 m and 111 m above the transducer head. The 1200 kHz RDI Workhorse was mounted on the lower part of the frame at approximately 2 mab facing downwards and was recording in 29 cells of 10 cm every 120 s, providing observations between the lander frame and the sea bed. The 2 MHz Nortek Aquadopp was mounted on the top of the frame as well (4 mab) and measured, looking upwards, in 20 cells of 50 cm each. With a blanking distance of 50 cm, it consequently provided complimentary, higher-resolution data to the 300 kHz RDI Workhorse in the range of 1 m to 10.5 m above the transducer head.

Once more, a JFE Advantech OBS was also mounted on one of the legs of the lander at roughly 1 mab and set-up to record every 120 s with a burst of 10 measurements at 1 Hz. Additional temperature records as well as complimentary salinity and pressure readings were supposed to be obtained with an additional Seabird SBE 37 Microcat but, due to unknown causes, the data retrieved from the instrument was corrupted.

2.3 Bathymetry Data

The bathymetric data used in this study was provided by the French Institute for Research of the Sea (Ifremer) via a high-resolution dataset on a 30-meter grid collected during various oceanographic campaigns such as the SARGASS (CREMER Michel, 2010) and PROSECAN 2 missions (Cirac, 2004), as well as several research cruises from the ITSAS (Cirac, 1998, 2001, 2002) and PLABAS series (Augris, 1993, 1994, 1995).

Apart from its application in visualising the research area (Figure 2.3), it also provided data on the bottom slopes of the thalweg. This information was used to calculate the wave steepness parameter introduced in Section 1.2.1. However, the trajectory of the thalweg needed to be determined first. For this, the dataset was converted into a digital elevation model by using ESRI's ARCGIS Pro software where the path of thalweg was identified by using the software's flow direction and accumulation tools. Next, the slope data along this trajectory was extracted and a running average over seven grid cells (corresponding to 210 m) was calculated. The resulting slope values could then be used to calculate the wave steepness parameter with equation 1.17.

Methods

This chapter introduces the methods used to answer the research questions laid out in Section 1.1. Since this study is based on *in-situ* observations, Section 3.1 will first detail the data processing steps that were applied to ensure reliable and usable data. The section is further split up into the different data quality control measures implemented for the acoustic Doppler current profilers (Section 3.1.1) and those for the optical backscatter sensors (Section 3.1.2). The section is concluded by details on how the data from the OBS sensors was correlated to measurements of sediment concentration to convert turbidity into suspended matter concentrations values (Section 3.1.3). The second part of this chapter is devoted to the basic working principles of the main data analysis techniques, namely those of Fourier and harmonic analysis (Section 3.2.1) as well as wavelet analysis (Section 3.2.2).

3.1 Data Processing

3.1.1 ADCP Data

This section describes the steps in the quality control procedures applied to the Nortek Aquadopp data as outlined in the instrument's manual (Section 1.1.9.3, p.43, Nortek Manuals (2017)).

The first step of the outlined procedure is to examine the roll and pitch of the instrument. This serves the purpose of identifying any large movements that might happen due to strong currents or objects hitting the instrument which could result in a shift of its location. Thresholds for excessive movement in tilt, roll or pitch were set at deviations of larger than 10 degrees No abnormalities could be detected during the stationary phase of the CTD as well as the deployments on the moorings and the bottom lander.

The most important step for ADCP data processing is the removal of any measurements where the backscatter intensity is below a predefined threshold. This threshold is also known as the noise threshold since it indicates where a signal within the data is no longer clearly discernible from background noise. The physical reasoning behind it is that from this point on, the Doppler shift can no longer accurately be measured. The typical profile of the backscatter intensity is an exponential decrease with distance from the transducer (Figure 3.1a). Under the assumption of no obstacles within the range of the beam, the signal will thus reach a point where it levels out. This level of nearly constant signal strength is called the noise floor. As long as the signal within a cell is above the noise floor, its measurement

(a) Average ADCP backscatter intensity

(b) Raw vs. despiked OBS turbidity signal
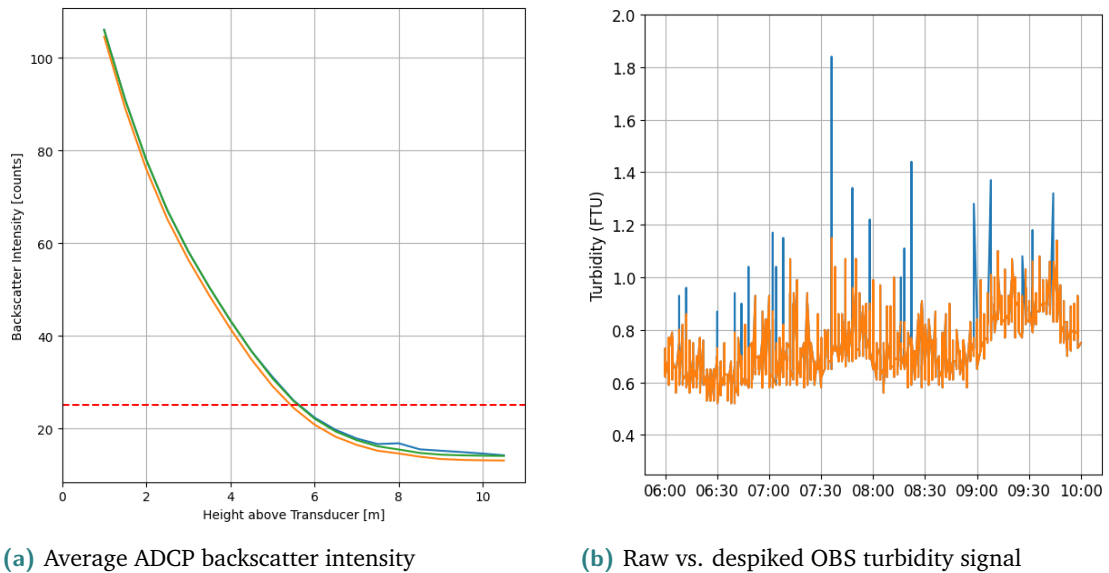
Fig. 3.1: Exemplary figures for the ADCP and OBS data processing methods. The left panel shows the time-averaged backscatter intensity measured with the upward-facing Nortek Aquadopp at the bottom lander. The dashed red line shows the implemented noise threshold with the different lines corresponding to each of the instrument's beams. The right panel shows raw (blue) and despiked (orange) turbidity data measured at the mooring deployed at 1000 m water depth for the indicated time frame on September 15, 2023.

can be seen as valid. If the signal strength falls below this threshold the measurements are not valid and can result in large, misleading values.

According to Nortek Manuals (2017), the noise threshold for a typical deployment is approximately 25 counts but also depends on the availability of particles in the water able to reflect the acoustic signal and can vary from instrument to instrument. For the application in this study, this typical case of 25 counts was chosen and validated by comparing the noise threshold to the exponential decay as a function of distance to the transducer head at all locations. An example profile for the Nortek Aquadopp located at the bottom lander is shown in Figure 3.1a. Lastly, it is important to note that due to the method of how the signal strength is computed internally, reliable data can still be retrieved from a few counts below the noise floor (Nortek Manuals, 2017). This means that the noise threshold set here can be considered to be a conservative value.

3.1.2 OBS Data

Optical backscatter sensors operate by illuminating the water with a light source and converting the backscattered light into a photocurrent. The amount of photocurrent, i.e. the strength of the signal, depends on the amount of particles in the sample but also on their shape, reflectivity and the characteristics of the medium itself (Downing, 2006). As the distribution of particles within the sample volume is random, the arrival of backscatter light to the detector is affected by random noise. If overall particle concentrations are low, as can be expected for the deep parts of Capbreton Canyon, this means that random noise

can make up a significant part of the overall signal. Additionally, the sensor has no way of knowing which kind of particles it is measuring, i.e. which object is actually scattering the emitted light back to the detector. This causes the sensor to also record small animals passing through the sampling window or even bits of seaweed. It is thus common practice to apply data processing techniques to denoise the signal.

In this study, denoising was done based on the normal deviate where any values are removed that exceed a threshold of three times the standard deviation calculated over a measuring window of 60 s. An example profile of the raw time series and the denoised signal from an OBS located at one of the moorings can be found in Figure 3.1b. This approach was found to still allow for significant turbidity increases to show in the resulting signal but also to be suitable to remove noise on smaller time scales. Mathematically, this approach can be written as:

$$z = \frac{X - \mu}{\sigma} \tag{3.1}$$

where:

- z is the normal deviate (or z-score).
- X is the observation of the time series.
- μ is the average of the 60 s moving window.
- σ is the standard deviation calculated over the 60 s moving window.

3.1.3 Correlation of Turbidity and Suspended Matter

This section will show how turbidity values were correlated to measured suspended matter concentrations (SPM) in order to convert turbidity values obtained at any OBS location to sediment concentrations. As mentioned in the previous section, the backscatter recorded by the OBS is influenced by a variety of particle characteristics such as its shape, size or density. Even when these characteristics are unknown, for many applications the assumption is valid that the particle characteristics remain similar throughout the research area. A common technique to then retrieve information on suspended matter concentrations from the OBS signal is to linearly relate them.

Here, the suspended matter concentration is retrieved by determining the dry-weight of filtered water samples taken with the CTD-Rosette system as laid out in Section 2.2.1. This dry weight corresponds to the suspended matter concentration within the water sample and can then be correlated to a corresponding turbidity measurement by the OBS mounted on the CTD frame taken at the same time. With the use of linear regression, this allows for the formulation of an equation that is able to convert turbidity into suspended matter concentrations under the assumption that the particle characteristics remain unchanged.

With multiple water samples taken during each CTD cast, retrieving the corresponding turbidity values from the OBS records was done automatically. Furthermore, the turbidity values had to be averaged over the 5-minute interval in which the CTD frame remained stationary due to their inherent noisiness discussed above. While the time of each water sample was recorded manually and in the ship logbook, the water samples were not always
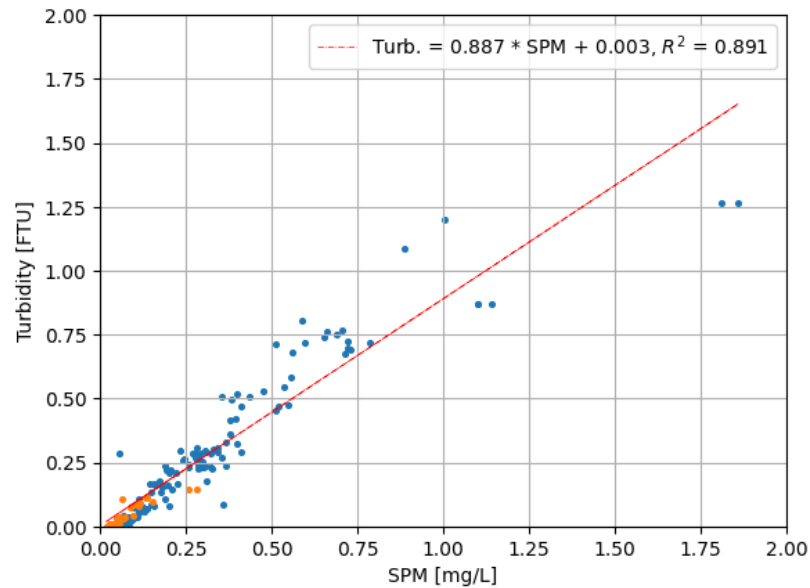
Fig. 3.2: Correlation of turbidity measured by the OBS located on the frame with suspended matter concentration (SPM) quantified from filter weights of water samples. The red line shows the relationship found between both variables using linear regression. Orange points highlight values where turbidity measurements were taken from an alternate OBS sensor positioned 1 meter above the CTD frame due to issues with the primary sensor.

taken at exactly the same time during this 5-minute window. Consequently, an averaging of the turbidity values from, for example, 2.5 minutes before and after the sampling time was not feasible, as this approach would average values where the CTD frame could already be moving again. With the CTD frame moving at 50 m per minute at maximum speed, a water sample taken at the end of the stationary window could then be related to turbidity values from as far as 125 m away.

To solve this issue, the measurement windows were numerically determined by using the plateaus in the pressure signal as indicators for when the CTD frame remained stationary. This was done by evaluating two standard deviations; one calculated in a moving window of 15 s before the current measurement and one evaluated for the 15 s after the current measurement. If both standard deviations fell below a threshold of 1 dbar (corresponding to less than 1 m of vertical excursion of the CTD frame in the 15 s before and after the measurement), the CTD frame was deemed to be stationary. Of course, this approach does not ensure that only one of these intervals is identified during each period of stationarity. It often occurred that multiple intervals were identified due to large vertical excursions of the ship causing either standard deviation to pass the 1 dbar threshold. This was solved by combining intervals that lie on the same pressure plateau by merging them into one interval if their respective start and end times fell within the same 5 minute period. The average time span of intervals retrieved this way was 4.99 minutes, highlighting the effectiveness of this method and visual inspection further ensured that no interval boundaries were incorrectly identified.

Having retrieved the correct time windows of turbidity measurements, the last step was to correlate them with the suspended matter concentrations where the `statsmodels` package (Seabold and Perktold, 2010) for Python was used to perform the linear regression. The result of this operation can be found in Figure 3.2. As discussed above, the location used for correlation was the OBS located at the CTD frame. Due to sensor issues, however, for a small number of time intervals, turbidity data from the OBS sensor mounted 1 m above the frame on the winch cable had to be used instead. The corresponding data points are marked orange in Figure 3.2. All in all, the following correlation was found:

$$\text{Turbidity [FTU]} = 0.003 + 0.887 * \text{SPM [mg/L]} \quad \text{with} \quad R^2 = 0.891 \tag{3.2}$$

3.2 Data Analysis

3.2.1 Fourier & Harmonic Analysis

Capbreton Canyon is a dynamic system where a variety of periodic processes — including waves, tides, and currents — interact with the canyon's complex topography. The interaction of tidal flows with this topography generates internal tides (see Section 1.2.3), which are a primary focus of this work. To effectively analyse these processes, which often exhibit characteristic frequencies (e.g. the M2 semidiurnal tidal frequency), it is crucial to apply mathematical tools capable of extracting and quantifying the presence of these frequencies. Two fundamental techniques that serve this purpose are Fourier analysis and harmonic analysis.

Fourier analysis is a method used to decompose a time signal into its constituent frequencies, revealing its spectral content. This technique is particularly useful when presented with complex, periodic signals where multiple frequencies are significant simultaneously, allowing the extraction of the most important frequencies that make up the signal. It is grounded in Fourier's theorem, named after the French mathematician Joseph Fourier (1768 - 1830), which asserts that any function $x(t)$ defined over an infinite interval can be uniquely represented by its corresponding spectral distribution. This is mathematically expressed as:

$$\hat{x}(f) = \int_{-\infty}^{\infty} x(t)e^{-2\pi i f t}\, dt \tag{3.3}$$

where:

- $x(t)$ is the original time series.
- $\hat{x}(f)$ is the Fourier transform of $x(t)$ representing the signal in the frequency domain.
- f is the frequency at which the Fourier transform is evaluated.
- t is time.
- $e^{-2\pi i f t}$ is the exponential function that oscillates at frequency f.

In essence, Fourier analysis transforms the signal from the time domain to the frequency domain. In this study, it is applied to identify the dominant frequencies present in observations of Capbreton Canyon, including pressure signals recorded near the canyon floor.

This provides valuable insight into the general tidal conditions within and above the canyon that ultimately shape the generation mechanism of internal waves. Additionally, it serves as the foundation for the more advanced Wavelet Analysis that will be introduced in Section 3.2.2.

Harmonic Analysis builds on the principles of Fourier analysis but focuses specifically on the contribution of individual frequencies to the time signal. Tidal frequencies in particular can be calculated very accurately due to the predictable nature of the gravitational forces by the Sun and Moon that cause them. Harmonic analysis can then be used to isolate and analyse the amplitude and phase of these specific tidal constituents within a time signal. Within this work, it is primarily applied in order to analyse the barotropic tidal conditions at the different research sites and to verify these findings against existing results (Section 4.1.2). This analysis provides further valuable insights into the generation mechanisms, particularly the dominant tidal conditions, that ultimately lead to the generation of internal waves.

When applied to measurements, equation 3.3 is technically no longer valid since the time series is not infinite. Instead, the time series of observations $y(t)$ is defined over the finite interval $[0, T]$ with its discrete time steps Δt determined by the sampling frequency f. However, Fourier postulated that this finite time series can still be represented by a linear combination of sine and cosine functions when the series is extended periodically (i.e., repeated infinitely). This enables the computation of the Fourier series, regardless, which approximates the original signal by using a finite number number of sine and cosine terms corresponding to harmonics of the fundamental frequency $\omega_1 = 2\pi/T$. With an infinite number of sine and cosine terms, the series converges to the original function. The length of the time series also determines the minimum and maximum frequencies that can be resolved with Fourier analysis. The minimum number of points necessary to resolve a periodic signal is three; one data point at the beginning, the zero crossing and the end of the signal. With the difference between data points Δt, the maximum frequency is thus given by $f_N = \frac{1}{2\Delta t}$, also known as the Nyquist frequency. With the same reasoning, the smallest resolvable frequency has a period of T itself and can thus be described by $f_{min} = \frac{1}{T}$. Ultimately, the resulting Fourier series is expressed as:

$$y(t) = a_0 + \sum_{n=1}^{\infty} C_n \sin(\omega_n t) + D_n \cos(\omega_n t) \tag{3.4}$$

where:

- $y(t)$ is the original time series.
- a_0 is the average of the time series over the interval $[0, T]$.
- $\omega_n = n\omega_1 = \frac{2\pi n}{T}$ is the frequency of n-th component as integer multiple of fundamental frequency ω_1.
- C_n and D_n are the Fourier coefficients that determine the amplitude of the sine and cosine components.
- n is the number of periodic components used to reconstruct $y(t)$.

The Fourier series can also be rewritten to explicitly show the amplitude and phase of each constituent:

$$y(t) = a_0 + \sum_n A_n \cos(\omega_n t - \varphi_n) \tag{3.5}$$

where:

- $A_n = \sqrt{C_n^2 + D_n^2}$ is the amplitude of the n-th component.
- $\varphi_n = \arctan \frac{C_n}{D_n}$ is the phase shift of the n-th component.

The contribution of each component to the original time series is calculated by assessing its impact on the overall variance of the data, also referred to as the power of that component. Mathematically, the power $P(f)$ at a frequency f is proportional to the square of the magnitude of the Fourier transform at that frequency:

$$P(f) = |\hat{y}(f)|^2 \tag{3.6}$$

The associated power spectrum contains information on how the energy of the original time series is distributed across the frequency domain. More specifically, peaks in the spectrum allow the identification of the dominant frequencies within the time series.

In the case of harmonic analysis, where the frequencies of the components are already known, the approach simplifies. In essence, it is reduced to a minimisation problem, where the goal is to minimise the error between the approximation using the desired frequencies and the original function. One common approach is to minimise the root mean squared error which is defined as:

$$RMSE = \sqrt{\frac{1}{N} \sum_{t=1}^{N} (y'(t) - y(t))^2} \tag{3.7}$$

where:

- RMSE is the root mean square error.
- N is the total number of observations.
- $y'(t)$ is the approximation of the original function at time t using the predetermined frequencies ω_n.
- $y(t)$ is the original time series of observations at time t.

In the scope of this study, harmonic and Fourier analysis were mainly used in Section 4.1.2 to establish the barotropic tidal conditions in the research area. For further details on these methods, readers are referred to common books on data analysis in physical oceanography, such as Thomson and Emery (2014) from which much of the material above was derived. Computationally, the harmonic analysis was carried out by using a Python-translated version of the well-established MATLAB package `UTide` (Codiga, 2011) while the Fourier analysis was implemented with the scientific computing package `SciPy` by Virtanen et al. (2020).

3.2.2 Wavelet Analysis

The previous section has introduced not only the significance of periodic processes in an oceanographic setting but also fundamental techniques of analysing them. A key prerequisite for using these methods, however, is that the frequencies within the signal are present throughout the time series. This poses significant challenges when features need to be analysed that are inherently intermittent such as internal waves. Since these are a primary focus of this work, the toolbox used in this study needs to be expanded with a technique that is able to retain information in both time and frequency domain in order to provide insight into which frequencies are present at which location in time. The underlying principle that separates the time and frequency domain is the well-known Heisenberg uncertainty principle which states that it is fundamentally impossible to achieve perfect resolution in both time and frequency domains simultaneously. Any method operating in both domains will consequently need to strike a balance between time and frequency resolution and the user will inherently need to accept a certain degree of error and "blur" in the results.

A method that is able to provide a solution to this problem, is **wavelet analysis**. With many procedures, software packages and approaches available, for this study an approach laid out by Torrence and Compo (1998) was chosen due to its availability through the Python package *PyCWT* (Krieger and Freij, 2023) and common usage in other studies on the subject (e.g. Ross et al., 2014; Jorda et al., 2013; Swart et al., 2011). The following sections give an introduction to this method including its basic working principle, necessary data preparations and significance testing once results have been obtained. The overall approach can be summarised into the following steps:

1. Preparing the data including detrending, demeaning and standardising.
2. Choosing a wavelet base function and scales.
3. Constructing the continuous wavelet transform.
4. Determining the Wavelet power spectrum.
5. Identifying the cone of influence and testing results for significance.

For further information on any of these steps or the method in general, the reader is referred to the previously mentioned work by Torrence and Compo (1998). A more theoretical treatment of the method can be found in Daubechies (1990).

In accordance with the method laid out above, the first step in wavelet analysis is **data preparation**. The primary goal here is to ensure that the time series which will be subjected to wavelet analysis, is sufficiently stationary, meaning that its statistical properties do not change over time. One example of non-stationarity would be the presence of a trend which would be included in the low frequency band of the wavelet analysis and thus might distort the results. Thus, common approaches to ensure stationarity are demeaning and detrending.

An additional data preparation step is to standardise the data which ensures that fluctuations within the data are as apparent as possible, enhancing the sensitivity of the wavelet transform to subtle variations and anomalies. By reducing the dominance of larger magnitudes, smaller yet significant variations are less likely to be overshadowed, allowing for

more accurate detection of patterns and anomalies. Thus, the data preparation process for this study involved these three steps:

1. **Demeaning**: The mean value of the time series is subtracted to stabilise the mean over time.

2. **Detrending**: A linear regression is applied to the data and the linear trend is subtracted from the time series to stabilise its variance.

3. **Standardisation**: The time series is standardised to ensure a standard deviation of one. This is achieved by using the normal deviate already introduced in Section 3.1.2 where the demeaned data of step 1 is divided by the standard deviation σ of the time series:

$$z = \frac{X - \mu}{\sigma} \tag{3.8}$$

Having prepared the data for analysis, the next step involves setting up the method by **choosing the base function and appropriate scales**. The key characteristic of a wavelet function is its short-lived oscillation localised in time. This means that in order to be admissible as a base function, a wavelet function must fulfil the following criteria: (1) an absence of a zero frequency component and (2) the possession of finite energy (Farge, 1992). Mathematically, these criteria for a wavelet function $\Psi_0(\eta)$ with dependence on the non-dimensional time parameter η can be formulated as follows:

1. Zero Mean, i.e. absence of zero frequency component: The positive and negative contributions to the total area underneath the curve should amount to zero.

$$\int_{-\infty}^{+\infty} \Psi_0(\eta)dt = 0 \tag{3.9}$$

2. Finite Energy, i.e. localised in time and space: After squaring the function, the total area underneath the curve should be a finite number.

$$\int_{-\infty}^{+\infty} |\Psi_0(\eta)|^2 < \infty \tag{3.10}$$

Due to the broad nature of these criteria, many functions are able to fulfil them. In this study, the Morlet wavelet was chosen for its universality and common use in other studies (e.g. Ross et al., 2014; Swart et al., 2011). It consists of a plane wave modulated by a Gaussian bell curve and is expressed as:

$$\Psi_0(\eta) = \pi^{(-1/4)} e^{i\omega_0\eta} e^{-\eta^2/2} \tag{3.11}$$

where ω_0 is the non-dimensional frequency, here taken to be 6 in accordance with (Farge, 1992) to satisfy the admissibility conditions.

Having chosen the wavelet function, it is also important to define the time scales on which the time series should be evaluated on. While they can be chosen arbitrarily, it is convenient to write them as fractional powers of two (Torrence and Compo, 1998):

$$s_j = s_0 2^{j\delta j}, j = 0, 1, \ldots, J \tag{3.12}$$

$$J = \delta j^{-1} \log_2(N\delta t/s_0) \tag{3.13}$$

Here, s_0 denotes the smallest resolvable scale and J determines the largest scale. The scales for this analysis were chosen to be $s_0 = 1$ h , $\delta j = 1/15$ and $J = 105$ h in order to adequately resolve semidiurnal tidal frequencies in the range from M2 (12.42 h) to M8 (3.11 h).

Using the base wavelet function and the scales, the time series can now be evaluated by **constructing the continuous wavelet transform**. At the core of wavelet analysis sits a fundamental mathematical operation called convolution. In essence, it involves the integration of two functions to produce a third function that expresses how the shape of one is modified by the other. In the context of wavelet analysis, convolution is used to compare different variants of the base wavelet function with the time series to determine how well the modified wavelet matches the signal. Expressed mathematically, this writes as:

$$(x * \Psi)(t) = \int_{-\infty}^{\infty} x(\tau)\Psi(t - \tau)\, d\tau \tag{3.14}$$

where:
- $x(t)$ is the original time series
- $\Psi(t)$ is the modified base wavelet function.

In wavelet analysis, this modified base wavelet function is also known as the "daughter" wavelet and represents a scaled and translated version of the base wavelet function (consequently also known as the "mother wavelet"). We can thus denote this daughter wavelet by its dependence on the translation parameter b and scaling parameter a :

$$\Psi_{a,b}(t) = \frac{1}{\sqrt{a}}\Psi_0\left(\frac{t - b}{a}\right) \tag{3.15}$$

where:
- b is the translation parameter.
- a is the scaling parameter.
- the normalisation factor $1/\sqrt{a}$ ensures that the wavelet remains normalised across different scales.

Here, the translation parameter b corresponds to the central time along which the focus of the wavelet analysis is shifted through the time domain. Modifications in the frequency domain are done by the scaling parameter a. Since it is inversely related to the frequency, it essentially modulates the base function by compressing and stretching it.

The convolution of the daughter wavelet at each combination of the scaling and translation parameter with the original time series, is then known as the continuous wavelet transform (CWT) and constitutes the key operation in wavelet analysis. If the right hand side of equation 3.14 is interpreted as a coefficient that is dependent on a and b, then the CWT can be written as:

$$W_x(a, b) = \int_{-\infty}^{\infty} x(t)\Psi_{a,b}^*(t)dt \tag{3.16}$$

where:

- $\Psi_{a,b}^*(t)$ is the complex conjugate of the daughter wavelet.

Using the CWT, a time series can now be analysed in the time and frequency domain. It is worth noting that performing the CWT is computationally more efficient in Fourier space since the convolution is reduced to a simple multiplication there (known as the convolution theorem). Thus, the following representation is usually used to compute the CWT for all time points simultaneously:

$$W_x(a, b) = \int_{-\infty}^{\infty} \hat{x}(f)\hat{\Psi}_a^*(f)e^{2\pi i f b}df \tag{3.17}$$

where:

- $\hat{x}$ and $\hat{\Psi}$ are the respective Fourier transforms.

Having transformed the time series, the next step is to visualise the results using the **wavelet power spectrum**. Similar to the Fourier power spectrum, the wavelet power spectrum shows how the power of different frequency changes over time and is computed as the square of the absolute value of the wavelet coefficients:

$$P(a, b) = |W(a, b)|^2 \tag{3.18}$$

An example of such a wavelet power spectrum based on observations from the mooring located at 500 m water depth is shown in Figure 3.3.

The introduction to this section has already mentioned that each wavelet analysis is inherently connected to a certain degree of "blur" due to the trade-off between time and frequency resolution. Since the signal is no longer completely transformed to the frequency domain (like in Fourier analysis) discontinuities at the edges also become important. This limitation is incorporated through the last step, the application of **significance testing** and the identification of the **cone of influence**. The cone of influence (COI) defines the regions where these edge effects caused by discontinuities are significant. In the wavelet power spectrum, the COI is usually visualised as a cone-shaped region around the edges of the time series, hence the name (see Figure 3.3). Any results within the cone of influence should be treated with caution as they may not accurately represent the time series. The width of COI is typically defined as the region where the wavelet power decreases by a factor of e^2 from its maximum value at each scale.
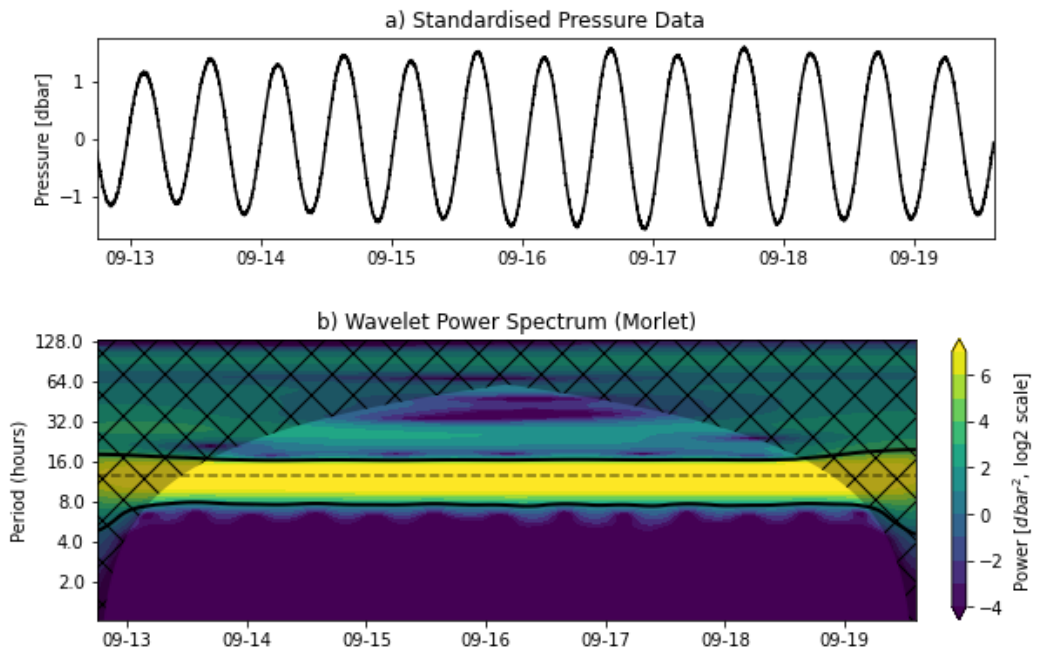
Fig. 3.3: Example of wavelet analysis applied to a time series. Here, the top panel corresponds to the standardised pressure signal recorded with the Nortek Aquadopp deployed on the mooring located in 500 m water depth. The bottom panel shows the wavelet power spectrum with the dashed line corresponding to the M2 tidal frequency and the hashed area corresponding to the cone of influence. Black contours show the 95% confidence interval.

Lastly, the results that do not fall into the cone of influence will still need to be tested for significance. With further details provided by Torrence and Compo (1998), the basic approach is to compare the observed wavelet power spectrum against a null hypothesis, typically a background spectrum that represents a random process such as white or red noise. Following a similar approach to Swart et al. (2011), a red noise spectrum was assumed as the null hypothesis for this study. The significance of the results is then determined by comparing the values of the power spectrum to those of the background spectrum. If the observed power surpasses a predefined 95% confidence level, the results are considered statistically significant (black contours in Figure 3.3).

Hydrographic Framework & Identification of Internal Tides

<div style="text-align: right; font-size: 2em;">4</div>

This chapter provides information on the key variables involved in investigating the internal tidal dynamics of Capbreton Canyon and identifying regions where sediment resuspension might be expected. First, the structure of the water column in and above Capbreton Canyon is examined with a specific focus on the water masses present (Section 4.1.1). This is followed by an exploration of the barotropic (Section 4.1.2) and baroclinic (Section 4.1.3) conditions influencing the research area by evaluating pressure, along-canyon velocity and temperature records obtained at the moorings and the bottom lander. The last section will focus on identifying regions of focused internal tidal energy (Section 4.1.4) by means of classifying the canyon into different regimes according to the value of the wave steepness parameter introduced in Section 1.2.1. The chapter is concluded by a discussion (Section 4.2) where the results are synthesised and the context is provided for the further investigation of nonlinear processes observed at the bottom lander discussed in the next chapter.

4.1 Results

4.1.1 Water Column Structure

Understanding the broader hydrographic setting which provides the boundary forcings to Capbreton Canyon, is crucial for interpreting the results of later sections. The general, vertical structure of the water column in the Bay of Biscay is characterised by distinct layers of different water masses, each with unique properties. Most of these water masses have their origin in the North Atlantic or are the result of the interaction of Atlantic waters with those originating in the Mediterranean (Gómez-Ballesteros et al., 2022). The goal of this section is to introduce the framework in which Capbreton Canyon is situated and to verify and analyse the local water column structure using the *in-situ* observations obtained there.

Overall, the water column structure above Capbreton Canyon is characterised by a well-mixed surface layer of approximately 50 m depth and deeper, more stable layers being separated by a permanent thermocline with strong temperature gradients. Within the Bay of Biscay three distinct water masses can be identified by their characteristic temperature and salinity profiles:
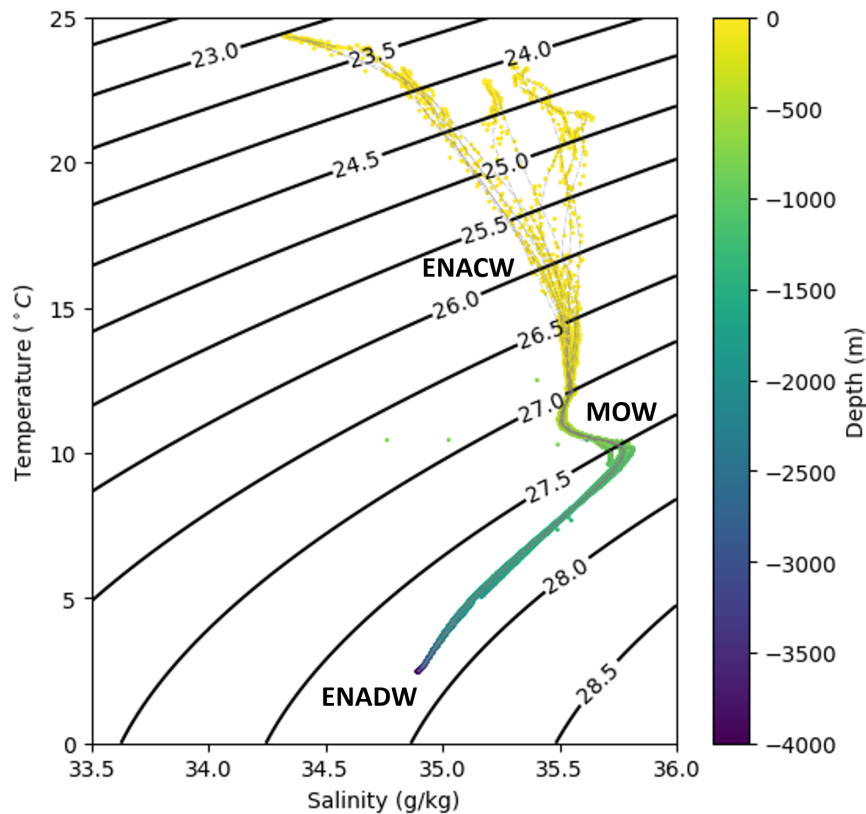
Fig. 4.1: Temperature-salinity (T-S) diagram showing the presence of three distinct water masses within the research area: (1) Eastern North Atlantic Central Water (ENACW), (2) Mediterranean Outflow Water (MOW), and (3) Eastern North Atlantic Deep Water (ENADW). The black contours depict the isopycnals and the colour gradient corresponds to the depth at which the measurements were taken. The grey-dashed lines correspond to the individual casts whereby only yo-yo casts in water depths deeper than 1000 m are visualised.

1. **Eastern North Atlantic Central Water (ENACW)**: Extending from below the well-mixed surface layer until about 1000 meter water depth, the ENACW is characterised by moderate temperatures (10°C to 15°C) and moderate salinities (35.2 to 35.8 practical salinity units (PSU)). It can further be subdivided into two water bodies; one with slightly cooler temperatures of subpolar origin (Harvey, 1982) and the other with slightly warmer temperatures of subtropical origin (Fraga et al., 1982). Due to this mixed origin, the properties of this water mass are dynamic and vary seasonally due to, for example, higher storm-induced mixing during the winter season (Pingree and Le Cann, 1992). Since the average depth of the continental shelf ($\approx$ 200m) falls within the range of this water mass, it is often involved in interactions with topography. The eddies and fronts that result are an important factor of ocean mixing and nutrient distribution within the Bay of Biscay (Bode et al., 2002).

2. **Mediterranean Outflow Water (MOW)**: Occupying depths between 700 m and 1300 m, this water mass is distinguished by high temperatures (around 10°C) and high salinities (35.5 to 38.4 PSU) due to its origin in the strongly evaporative climate of the Mediterranean Sea (Baringer and Price, 1997). Highest salinities are found immediately after its exit from the Mediterranean in the Straight of Gibraltar whereas

values in the Bay of Biscay are significantly lower due to mixing with surrounding waters. The MOW introduces a third, intermediate layer between the colder, fresher water mass above and the deeper, denser waters below. Through this layering effect, it plays an important role in the overall stability of the water column, vertical mixing and nutrient distribution within the Bay of Biscay.

3. **Eastern North Atlantic Deep Water (ENADW)**: Below the MOW sits the Eastern North Atlantic Deep Water (ENADW) which occupies the deep bottom waters within the Bay of Biscay below 2000 m water depth. In some areas in the Bay of Biscay, Labrador Sea Water (LSW) may also appear near the lower end of the MOW but tends to merge with the MOW, consequently becoming difficult to discern as a separate water mass (van Aken, 2000). Overall, the ENADW is characterised by low temperatures (2°C to 4°C) and high salinities (around 35 PSU). It enters the Bay of Biscay as part of the broader deep Atlantic circulation and is formed both by the Northeast Atlantic Deep Water (NADW) and the Antarctic Bottom Water (ABW) (Mulder et al., 2012). The cold, dense nature of the ENADW makes it a significant factor in the overall stability of the water column and the deep-water circulation of the Bay of Biscay.
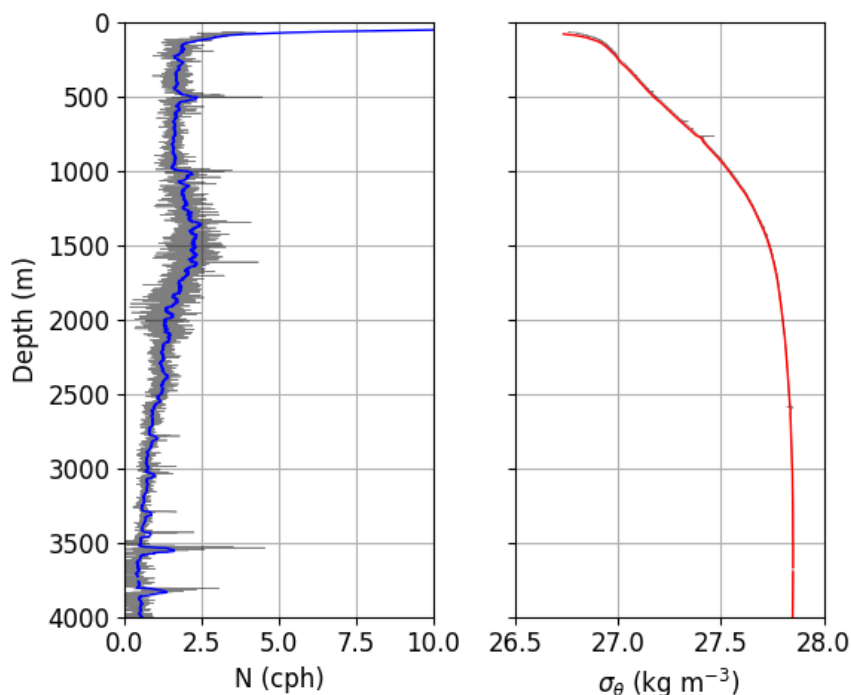
Fig. 4.2: Profiles of buoyancy frequency N (left) and potential density anomaly (right) in depths from 50 m to 4000 m. The blue line in the left plot shows a moving average of 30 m increments with the grey area showing the average over all research sites per 1 m depth bin. Note that the large variabilities in N below 3500 m may be caused by data limitations as only two single casts reached below this depth.

Using the knowledge of the water masses present within the Bay of Biscay, the focus can now be laid on evaluating the stratification of the water column above the canyon. For this, the buoyancy frequency was calculated from absolute salinity, conservative temperature and sea pressure measured by the CTD following the approach of the Intergovernmental Oceanographic Commission et al. (2010) and implemented in the Python package `gsw`. The resulting profile, and that of the derived potential density anomaly, can be seen in Figure 4.2.

The profile of the buoyancy frequency shows several interesting features throughout the water column. Although the shown profile does not extend further upwards than 50 m below the surface, the profile still shows high stratification levels in these depths indicating a well-defined thermocline in this region. As depth increases, the buoyancy frequency generally decreases, indicating weaker stratifications in deeper layers. Notably, in depths between 1000 m to 1800 m, N increase once again indicating a permanent pycnocline in this region. This is due to the MOW present in these depths causing the stratification to temporarily increase due to the higher densities of this water mass and the resulting strong density gradients. This is followed by a steady decrease in values of N towards the bottom, suggesting a weakly stratified deep ocean which is to be expected as Figure 4.1 shows colder more homogeneous water masses at these depths, namely the ENADW / LSW.

The potential density anomaly profile shows a stable water column as high density waters are located below less dense waters. The steep gradient near the surface also supports the existence of a well-defined thermocline and the steady decrease thereafter reflects a uniform water mass between the permanent thermocline and the permanent pycnocline. The permanent pycnocline can also be identified in this profile as the region between 1000 m to 1500 m where the profile 'bends', i.e. a steady change in density gradient is visible. At depths greater than 1500 m the density gradient becomes more uniform once again, indicating the presence of a homogeneous water mass, here the ENADW.

4.1.2 Barotropic Conditions

This section will briefly introduce the results of Fourier and harmonic analysis applied on the pressure data obtained at the mooring and the bottom lander. Although retrieved near the bottom, pressure changes recorded there are still dominated by the overall tidal movement so the signal can be interpreted to predominantly depict barotropic tidal conditions. These conditions within the Bay of Biscay are well-established through observations and numerical simulations and first order dynamics have been found to be largely dominated by barotropic semidiurnal tides (Le Cann, 1990). The following paragraphs will thus aim to verify these findings and the results are further discussed in Section 4.2.

The results of the Fourier analysis applied on the pressure data are shown in Figure 4.3 and indicate that barotropic conditions are dominated by the principal semidiurnal component (M2). The relative thickness of each of the peaks in Figure 4.3 can be attributed to the availability of approximately one week of data. Nonetheless, the power attributed to this component remains relatively uniform throughout the measurement stations, indicating
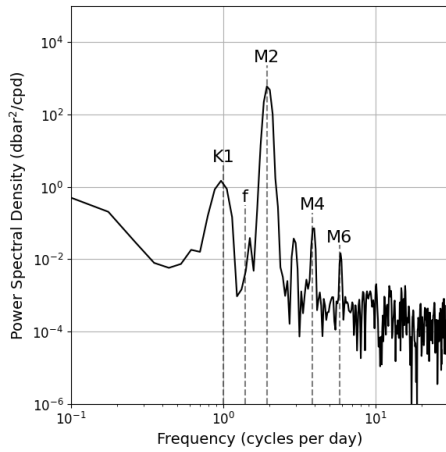
(a) Mooring 1 (500 m water depth)
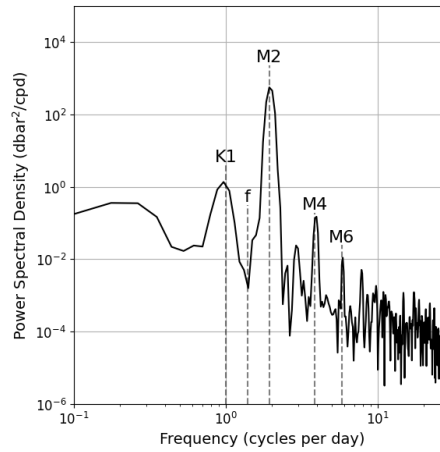
(b) Mooring 2 (1000 m water depth)
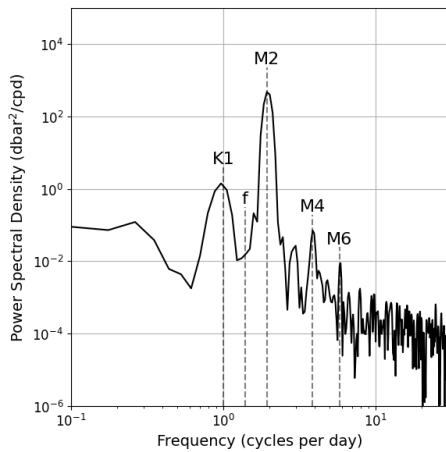
(c) Mooring 3 (1500 m water depth)

(d) Bottom Lander (2500 m water depth)

Fig. 4.3: Power spectrum of the pressure recorded at the moorings and the bottom lander by the Nortek Aquadopp. Black lines show the power spectrum with dashed lines corresponding to the principal diurnal component (K1 ≈ 23.93 h), the inertial frequency (f ≈ 17.33 h), the principal semidiurnal component (M2 ≈ 12.42 h) and higher semidiurnal harmonics (M4 ≈ 6.21 h, M6 ≈ 4.14 h).

spatially uniform barotropic tidal conditions. The second most important tidal constituent is the principal diurnal component (K1), with power values being roughly two orders of magnitude smaller than those of the M2 tidal frequency. A peak at the inertial frequency was only found at the deployment location of the bottom lander (2500 m depth) while no such signal could be found at any of the moored sites (500 m, 1000 m, 1500 m depth).

These findings are further supported by results of the harmonic analysis which showed an amplitude of the M2 tide between 1.48 to 1.58 m whereas the K1 component only had amplitudes ranging between 0.04 m and 0.08 m. Higher harmonics of the semidiurnal tide, namely M4, M6 and M8, were found to not be significant with amplitudes ranging between a few millimetres in the case of the M8 tidal frequency to a maximum 4 cm in the case of the M4 tide. Evaluations of the phase differences in the arrival of the M2 tide with reference to the bottom lander, further supported the findings of a nearly uniform M2 tide with the largest difference – from the bottom lander at 2500 m water depth to mooring 1 at 500 m water depth – being covered in only five seconds, equivalent to a phase difference of 0.04 degrees.

4.1.3 Baroclinic Conditions along the Thalweg

Due to the focusing of energy near the seafloor, internal waves propagating within a submarine canyon often show increased levels of bottom velocities. Confined by the topography of the canyon and often generated by the barotropic tide, these focused and amplified internal waves manifest as increased bottom velocities in the along-canyon direction, with a periodicity associated to the dominant tidal frequency, in this case the principal semidiurnal component (M2). At this point, due to a lack of observations of surface currents, it is not possible to say whether the observed velocities are indeed enhanced. However, finding evidence of tidal frequencies in both along-canyon velocity and temperature as well as evidence of their intermittent character, give good first indications of the presence of internal tides. The possible enhancement of along-canyon velocities will be discussed in Section 4.2 by putting them into context with high-frequency radar observations reported by Caballero et al. (2020). Overall, the wavelet analysis of both variables, shown in Figures 4.4 and 4.5, reveals significant signals of internal tides with notable differences between depths.

Wavelet analysis of the shallowest research site at 500 m water depth (Figures 4.4a and 4.5a) show little influence of the M2 tidal frequency on both the along-canyon velocity and the temperature profile recorded at 1 metre above bottom (mab). While being intermittently significant, especially on September 17, in the along-canyon velocity, no significant M2 influence could be found in the temperature profile throughout the measurement period. In fact, the wavelet analysis of the temperature profile showed virtually no periodicity on an hourly scale at all apart from small, isolated instances of higher harmonics and other high frequency signals. For the along-canyon velocity the higher semidiurnal harmonics, especially the M4 harmonic, showed higher importance than the M2 tide but again only intermittently, here for about half the measurement period between September 16 and 20, 2023.
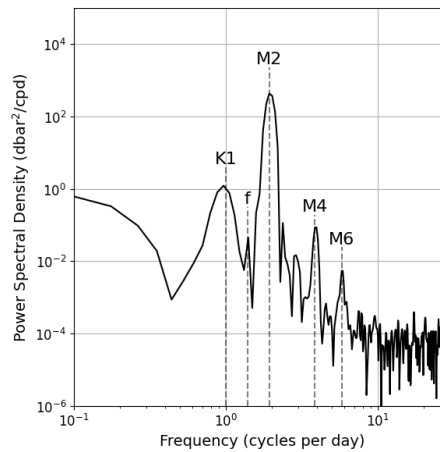
(a) Mooring 1 (500 m water depth)

(b) Mooring 2 (1000 m water depth)

(c) Mooring 3 (1500 m water depth)

(d) Bottom Lander (2500 m water depth)
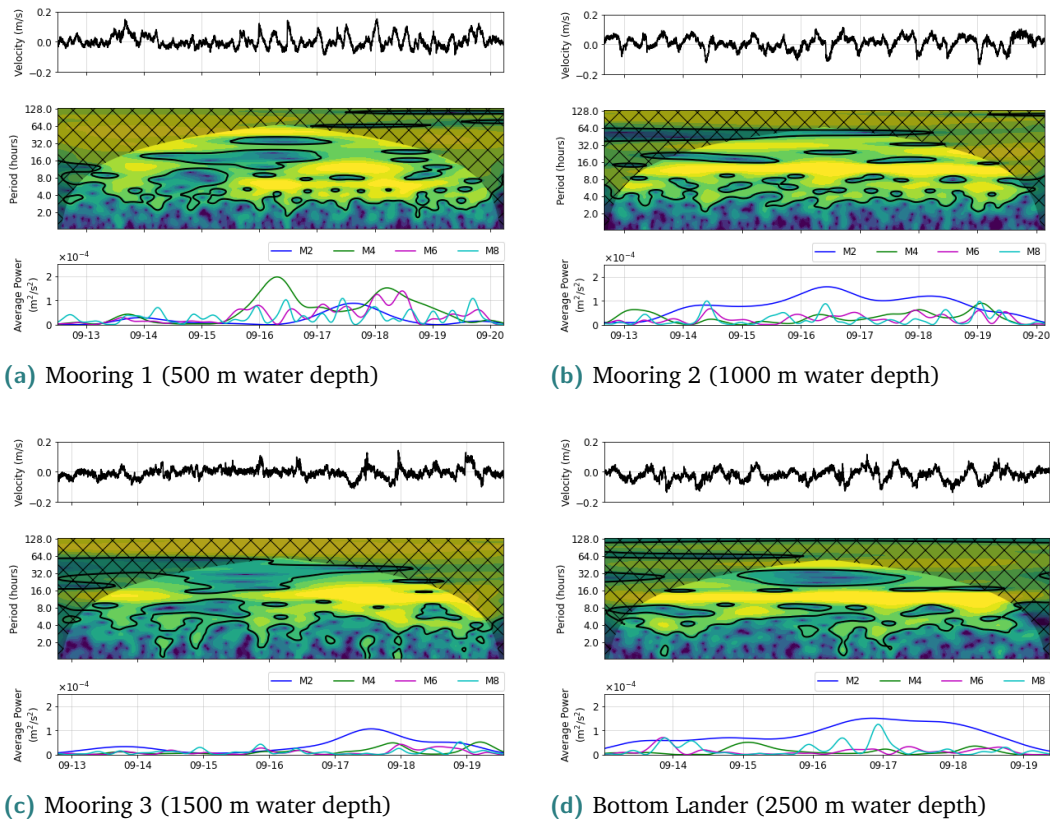
Fig. 4.4: Wavelet analysis of the along-canyon velocity at the moorings and the bottom lander. The top panel of each figure shows the raw time series of the along-canyon current velocity. The middle panel shows the corresponding wavelet power spectrum where yellow colours represent large values and blue colours represent low values. The colouring scale was left unchanged for all plots. Black contours visualise the 95% confidence level as defined in Section 3.2.2 with encircled yellow regions deemed significant. The bottom panel shows the average power corresponding to a selection of semidiurnal tidal frequencies (M2, M4, M6, M8).

500 m deeper, at the mooring in 1000 m water depth, wavelet analysis reveals a different situation for the along-canyon velocity but a similar picture for the temperature profile as shown in Figures 4.4b and 4.5b. Again, the temperature profile shows virtually no dependence on an hourly scale with few exceptions in the period range between 1 and 4 hours and one significant M2 event on September 16, 2023, however with little power values associated to it. The along-canyon velocity, on the other hand, shows a high significance in the M2 period throughout the measurement period. Higher harmonics are still significant throughout the time window too, but overall, M2 dominates the average power explained by semidiurnal frequencies.

The deepest mooring, located at 1500 m water depth, shows another situation again, with M2 being the overall most important semidiurnal component but being only intermittently present in both signals and significance in along-canyon velocity occurring at a different time than in the temperature profile. In the case of the temperature profile, M2 significance occurs on September 15 with three distinct peaks in temperature profile during this period. In the case of the along-canyon velocity, the most significant period occurs on September 17

(a) Mooring 1 (500 m water depth)

(b) Mooring 2 (1000 m water depth)

(c) Mooring 3 (1500 m water depth)

(d) Bottom Lander (2500 m water depth)
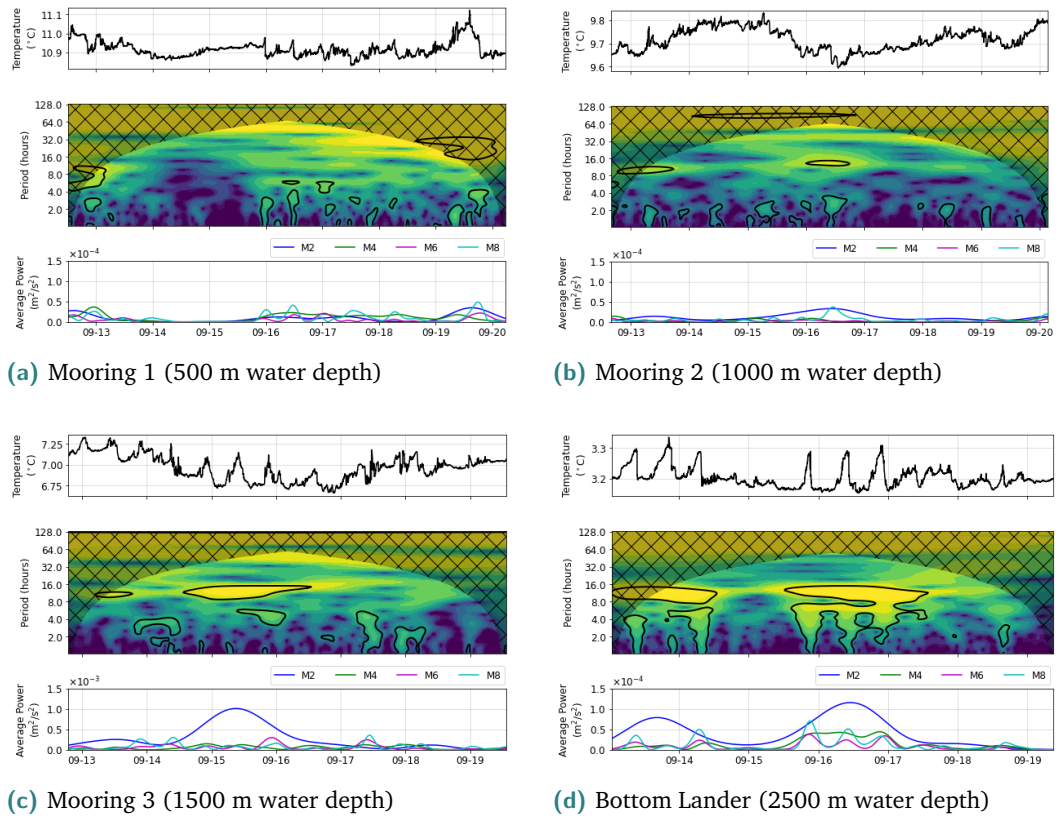
Fig. 4.5: Wavelet analysis of the temperature records obtained at the moorings and the bottom lander. The top panel of each figure shows the raw time series recorded with the OBS located at 1 mab. The middle panel shows the corresponding wavelet power spectrum where yellow colours represent large values and blue colours represent low values. The colouring scale was left unchanged for all plots. Black contours visualise the 95% confidence level as defined in Section 3.2.2 with encircled yellow regions deemed significant. The bottom panel shows the average power corresponding to a selection of semidiurnal tidal frequencies (M2, M4, M6, M8). Note the different scale of the y-axis in the bottom plot corresponding to mooring 3 (subfigure (c)).

and, while still significant, average power attributed to the M2 frequency remains small otherwise.

The most complete picture of internal tides in both the velocity and temperature time series is recorded at the bottom lander at 2500 m water depth as shown in Figures 4.4 and 4.5. Both signals show a strong presence of the M2 tidal frequency, with a significant, strong signal showing persistently throughout the measurement period in the case of the along-canyon velocity and intermittently in the temperature series during two events. Especially, the results of the wavelet analysis of the temperature series are interesting as each occurrence of an M2 tidal signal correspond to gradual increases and sharp drops in temperature and each temperature drop is further accompanied by the presence of higher harmonics. If the recorded bottom velocities now also show to be enhanced (which will be discussed in Section 4.2), then these signatures in temperature combined with the strong tidal signal in current velocity, provide strong indications for the presence of (nonlinear) internal waves at this location.

4.1.4 Regions of Internal Tide Focusing

In order to evaluate the wave steepness parameter with equation 1.17, the local conditions within Capbreton Canyon needed to be quantified first. These include the local seafloor slope s_b, the dominant internal wave frequency ω_b, the Coriolis frequency f and the buoyancy frequency N. The slope of the seafloor was derived from the high-resolution bathymetry data provided by Ifremer (see Section 2.3). The internal wave frequency was taken to be the M2 frequency, in line with the findings of the previous section where the barotropic signal was found to be predominantly influenced by the M2 tidal component. The vertical profile of the buoyancy frequency was already introduced in Section 4.1.1. The results for the wave steepness parameter along the thalweg of Capbreton Canyon are presented in Figure 4.6. This figure both includes the bathymetric profile of the canyon and the calculated wave steepness parameter as a function of distance along the thalweg from the first research site at 500 m water depth from which buoyancy frequency information is available.

The key findings can be summarised corresponding to the three criticality regimes introduced in Section 1.2.1:

1. **Supercritical Regions ($\alpha > 1$):**

   - The analysis shows that the shallower regions of Capbreton Canyon (above approximately 2200m) predominantly fall into the supercritical regime. This suggests that internal waves in these areas are reflected, resulting in horizontally, standing and downward propagating wave-like patterns.

2. **Subcritical Regions ($\alpha < 1$):**

   - Conversely, the deeper regions of Capbreton Canyon beyond 2800m water depth can be classified as subcritical. Here, internal waves are thus reflected forward, possibly leading to a focusing of internal wave energy further into the canyon.

3. **Critical Regions ($\alpha = 1$):**

   - Between approximately 2200m and 2800m, the wave steepness parameter indicates a near-critical regime. While intermittently deviating from critical values (shown as the grey bar in 4.6), this region can be expected to show elevated levels of internal wave energy with the possibility of internal wave breaking and enhanced turbulence.

Conclusively, the shallower regions where the moorings are located (shown as stars in figure 4.6) fall predominantly within the supercritical regime. The bottom lander, on the other side, is situated near a region of critical values all the while showing supercritical values exactly at its location. More importantly, it sits at the transition point from the subcritical to the critical regime. This makes it a possible location for internal wave breaking to occur and makes it a promising site for further investigation into the potential for internal wave-induced sediment resuspension.
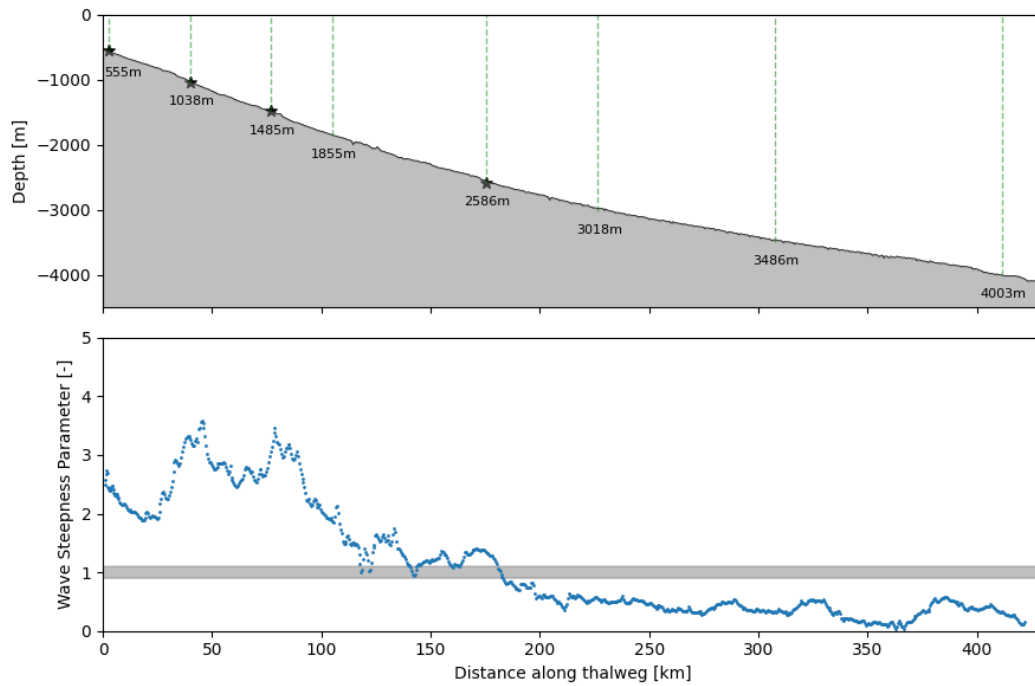
Fig. 4.6: Bathymetric profile and wave steepness parameter along the thalweg of the canyon. The upper panel shows the thalweg profile as a function of depth and the locations of the moorings and the bottom lander indicated by stars. The vertical green dashed lines indicate the locations where CTD profiles were taken. The lower panel shows the wave steepness parameter where the near-critical region is highlighted with grey shading.

4.2 Discussion

The goal of this chapter is to establish the hydrographic framework in which Capbreton Canyon is located, to describe the barotropic conditions, to identify internal waves in the observations of nearbed along-canyon velocity and temperature and ultimately to identify potential hotspots of sediment resuspension due to focused internal wave energy.

A key part of the hydrographic framework was established by describing the water masses present within the research area by using observations of the CTD along the canyon axis. Results correspond nicely to those found in the literature and show the presence of three distinct water masses: the ENACW, the MOW and the ENADW. Calculation of the buoyancy frequency and measurements of the potential density anomaly show a stable water column with a well-pronounced thermocline and a permanent pycnocline located at approximately 1500 m water depth.

Barotropic conditions were found to be largely in accordance with findings of other studies such as the results of numerical experiments by Karagiorgos et al. (2020) who also found the M2 tidal frequency to be dominant with a similar amplitude range in the region of Capbreton Canyon of roughly 1.4 m. Furthermore, the barotropic tide showed spatial uniformity with small phase differences between each of the evaluated locations suggesting small surface

current magnitudes due to only small differences in sea surface elevation caused by the tidal wave. This is supported by observations by Caballero et al. (2020) who used high-frequency radar to capture surface current in the south-eastern corner of the Bay of Biscay. The authors of the study found average surface current values in the order of a few centimetres per second, much smaller than bottom velocities found near the seafloor at the moorings or the bottom lander, where especially at the latter velocity magnitudes where on average 11.6 cm/s.

Together with the knowledge of enhanced bottom velocities, internal wave signals could then be identified by applying wavelet analysis on the time series of along-canyon velocity and temperature obtained at the moorings and the bottom lander. Results show a varying degree of semidiurnal tidal influence suggesting complex baroclinic conditions with an overall increase of importance of higher semidiurnal harmonics as depth decreases. This represents a similar finding to that of Alberty et al. (2017) who also report a decrease in the M2 importance and a subsequent increase in its higher harmonics in La Jolla Canyon off the west coast of the United States, suggesting nonlinear tidal interactions with supercritical topography as the cause of this shift. Furthermore, observations at the mooring in 1500 m water depth show two significant M2 periods not occurring at the same time suggesting two separate internal tide events. This is in line with results by Rainville et al. (2010) who were able to show that internal tides from multiple generation sites interact with each other causing complex patterns of constructive and destructive interference. The location with the most variance of the original time series explained by the M2 tide was found to be the bottom lander at 2500 m water depth. Here, two distinct periods of M2 significance were found in the temperature profile, characteristic of the intermittent nature of internal waves. The associated emergence of higher harmonics during each event suggest the presence of nonlinear effects such as wave steepening or wave breaking.

These findings are further supported by the results of the wave steepness parameter calculations where internal tide energy was found to be focused near the bottom lander due to its location in a near-critical region for semidiurnal internal tides. Furthermore, the results showed that the upper parts of Capbreton Canyon in depths shallower than approximately 2200 m water depth fall within the supercritical regime and depths below 2800 m water depth fall within the subcritical regime.

Overall, these findings provide an important context for the detailed observations of nonlinear waves at the 2500 m site discussed in the next section where their connection to sediment resuspension will be explored. It is important to note, however, that many of the obtained results are limited by important assumptions and can thus not be considered as universal. An example of this, is the reflection of internal waves along the supercritical side walls of Capbreton Canyon as touched up in Section 1.2.1. While sufficient information is available to calculate the wave steepness parameter for the entire canyon, velocity and turbidity measurements are only available along the thalweg. As a result, this study could only focus on the dynamics near the thalweg and needs to acknowledge that the observed dynamics are not solely caused by the local conditions. For instance, previous findings by Vlasenko et al. (2016) have shown that the proximity of steep sloping sidewalls in a

three-dimensional canyon can alter the behaviour of internal waves, potentially increasing turbulence and enhancing sediment resuspension near these walls as well.

Taking all these considerations into account, this chapter has successfully identified the 2500 m site where the bottom lander was deployed as a site of strong internal wave activity and a possible hotspot for sediment resuspension. Observations presented in the next chapter will confirm these results and present evidence of nonlinear internal wave breaking, the presence of an internal tidal bore and explore the sediment resuspension observed there.

Sediment Resuspension by Nonlinear Internal Waves

<div align="right">

5

</div>

5.1 Results

This chapter will explore observations of nonlinear internal wave breaking at the location of the bottom lander at 2500 m water depth and its connection to resuspension of sediment. In the first section, two different regimes of internal wave breaking are introduced where one shows internal waves in their shoaling phase whereas the other shows indications of the breaking phase, more specifically the formation of an internal tidal bore (Section 5.1.1). The second section subsequently focuses on observations of particle concentrations during and after the passage of the internal tidal bore, exploring the effects on resuspension and transport of sediment during this event (Section 5.1.2).

5.1.1 Two Regimes of Internal Waves

The main focus of this section is on the classification of observations obtained at the bottom lander into two distinct regimes of internal wave breaking. An overview of the observations used for this can be found in Figure 5.1. Here, Roman numbers and their coloured frames correspond to four distinct periods (I to IV) that can be classified into two different regimes of internal wave breaking (red and yellow). The following paragraphs will introduce the basis on which this classification was made and highlight the main similarities and differences between each regime and each of the periods.

A universal feature within the observations is the periodic flow reversal as seen in the periodic shift in colour in the velocity direction plot in Figure 5.1b, which happens at a similar frequency to that of the M2 tidal constituent. Furthermore, each upcanyon flow phase, indicated by blue colours, is accompanied by either short bursts or consistently higher flow velocities, indicated by red values in Figure 5.1a. More specifically, upcanyon flow velocities reach magnitudes exceeding 22 cm/s whereas their downcanyon counterparts only reach values of up to 12 to 14 cm/s. Interestingly, this concludes the observed similarities as neither the vertical velocities or acoustic backscatter recorded from the ADCP nor the sediment concentration and temperature recorded by the OBS, show further coherent structures spanning the entire data set.

The classification into the two regimes is based on distinct differences in the temperature signal as well as more subtle periodic differences in the current velocity signal.
Starting chronologically, the yellow regime is the first to be observed between the start of
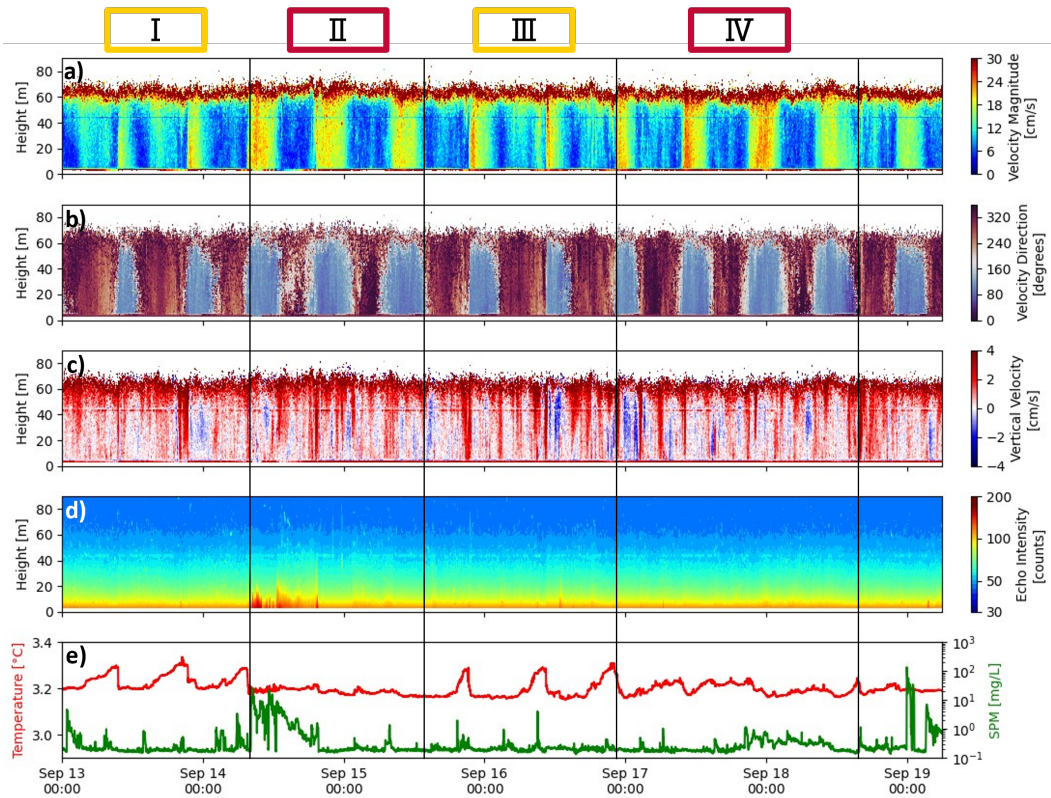
Fig. 5.1: Observations used to investigate the presence of nonlinear internal wave breaking at the bottom lander from September 13 - 19, 2023. The subplots represent: a) velocity magnitude in cm/s, b) velocity direction in degrees, c) vertical velocity in cm/s, d) acoustic backscatter in counts, and e) temperature and suspended matter concentration (SPM) at 1 mab. Generally, red colours correspond to large values whereas blue colours correspond to low values. The velocity direction is measured counterclockwise relative to East (0 degrees) where red colours indicate downcanyon flow and blue colours indicate upcanyon flow. Velocity parameters as well as acoustic backscatter were recorded by the RDI Workhorse whereas suspended matter concentration and temperature were recorded by an OBS.

the observations on September 13 and approximately September 14, 7:00, and reoccurring from September 15, 13:00 to September 17, 2:00. The main feature of the yellow regime is its characteristic temperature profile of a gradual increase during the downcanyon flow phase, followed by a sharp temperature drop as the flow reverses (see Figure 5.1e). As the wavelet analysis of the temperature record has shown (see Section 4.1.3), each of the temperature drops occurs with a semidiurnal tidal frequency, mainly corresponding to the principal component, M2. This is in stark contrast to the temperature records during the red phase, which will be introduced shortly, where no such signal is visible.

Another key feature of the yellow regime is its cross-canyon flow component. This is better visualised in Figure 5.2 where each yellow phase shows a significant tidal excursion in the cross-canyon direction of roughly 1 km per tidal cycle, most notably during period I. Again, this is absent during the red regime. Further evaluating the flow direction, Figure 5.1b also allows for the identification of asymmetry in the length of down- and upcanyon flow phases as the blue areas (indicating upcanyon flow) are much narrower, and thus shorter, than the
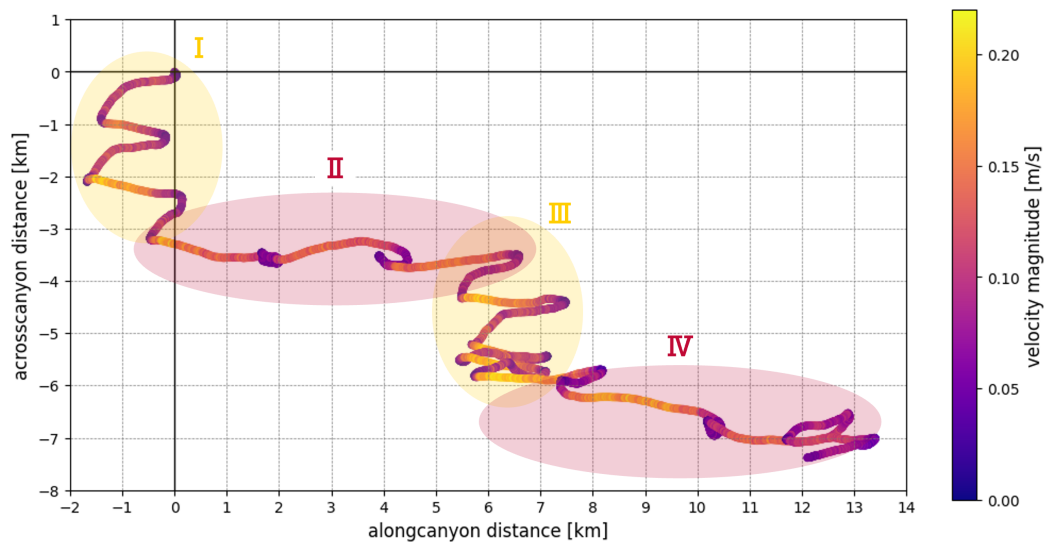
Fig. 5.2: Progressive vector plot of depth-averaged current measurements recorded by the Nortek Aquadopp mounted on the bottom lander frame. Colouring as well as Roman numbers correspond to the regimes defined in Figure 5.1.

red areas (indicating downcanyon flow). This is most pronounced during period I but also clearly visible during period III. Once more, this is in contrast to the red regime where the opposite is observed: longer upcanyon and shorter downcanyon flow phases.

The red regime is observed from September 14, 7 am to September 15, 1 pm and from September 17, 2 am to September 18, 4 pm. The key characteristic of the red regime is a strong, prolonged upcanyon flow combined with little backflow during downcanyon periods (see Figure 5.1a). It is during this regime where the record shows the previously mentioned high flow velocities in the upcanyon direction, regularly exceeding 22 cm/s. For the direction of this flow, Figure 5.2 is once again better suited, showing that it almost exclusively travels in the alongcanyon direction, especially during period II. Similar to the yellow regime, investigations of the flow direction in Figure 5.1b show an asymmetric profile where the downcanyon flow (indicated by red colours) is significantly narrower than the upcanyon flow (indicated by blue colours), most notably during period II. In contrast to the yellow regime, however, flow velocities are also significantly decreased during the downcanyon flow phase with velocities rarely exceeding 6 cm/s for prolonged periods of time. Lastly, while the yellow regime showed pronounced temperature signals, the red regime is characterised by a comparatively flat temperature profile without large excursion, again most notably during period II.

5.1.2 Sediment Resuspension by Internal Tidal Bore

The main objective of this section is to investigate the internal tidal bore observed at the bottom lander between September 14, 7:30 am and 7:30 pm and its influence on sediment resuspension (see Figure 5.3). The underlying hypothesis of this section is that internal tidal bores, formed by nonlinear wave breaking, are able to resuspend sediment through enhanced levels of turbulence during its passage. Hereafter, the first feature at 7:30am is
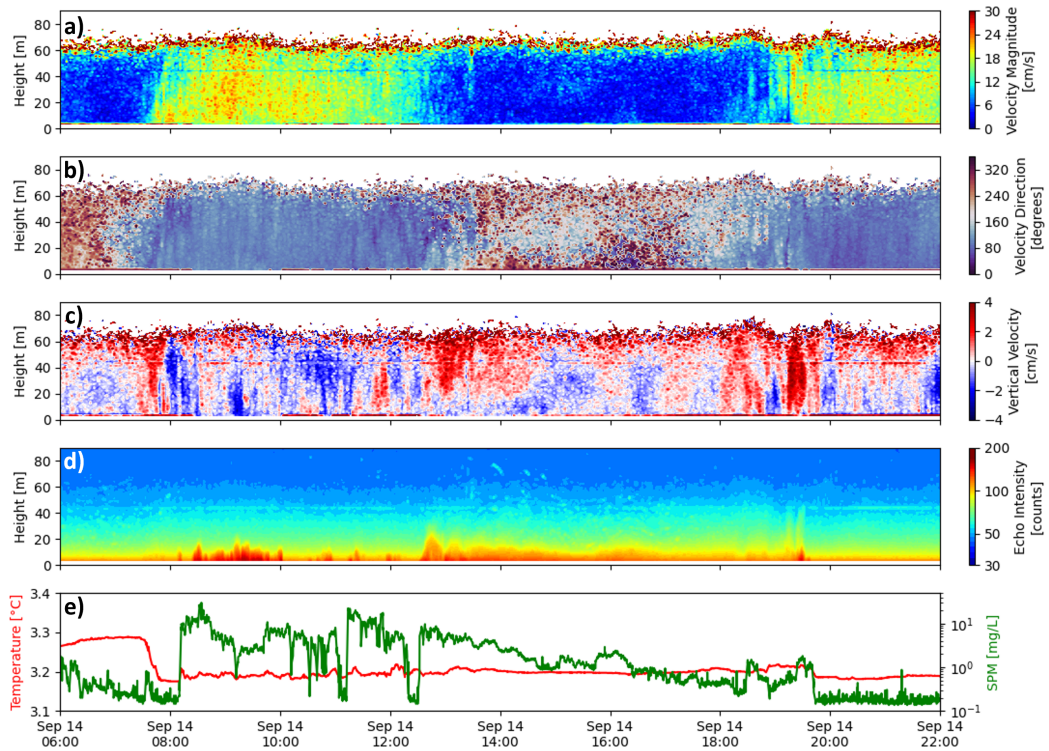
Fig. 5.3: Observations of two internal tidal bore features passing the bottom lander on September 14, 2023. The subplots represent: a) velocity magnitude in cm/s, b) velocity direction in degrees, c) vertical velocity in cm/s, d) acoustic backscatter in counts, and e) temperature and suspended matter concentration (SPM) at 1 mab. Generally, red colours correspond to large values whereas blue colours correspond to low values. The velocity direction is measured counterclockwise relative to East (0 degrees) where red colours indicate downcanyon flow and blue colours indicate upcanyon flow. Velocity parameters as well as acoustic backscatter were recorded by the RDI Workhorse whereas suspended matter concentration and temperature were recorded by an OBS.

consequently referred to as "Bore 1" and the one at 7:30pm as "Bore 2". The main focus will lie on Bore 1 since it shows the most pronounced sediment response while Bore 2 seems to only interact with the sediment response caused by Bore 1 without actively resuspending sediment itself.

The leading edge, or "head" of Bore 1 passes the bottom lander on September 14, 2023 at approximately 7:30 am and is accompanied by a sharp increase in velocities (Figure 5.3a), sharp drop in temperatures by approximately 0.11 °C (Figure 5.3e) and by an abrupt change in velocity direction from predominantly downcanyon (red) to predominantly upcanyon (blue) (Figure 5.3b). Furthermore, the bore moves in at the bottom first where an increase by more than 10 cm/s is realised in less than 20 minutes. Using this 10 cm/s threshold to also evaluate the time difference between the bottom and the top of the feature, the time delay amounts to roughly 20 minutes as well, after which the entire measured water column up to approximately 60 m is characterised by significantly higher current velocities.
The vertical velocity component (Figure 5.3c) shows strong upward motion just before the velocities increase, followed by downward motion immediately afterwards. Together with

the time delay between the arrival of the bore in the lower water levels and the higher water levels, this indicates the presence of a rotor within the head of the bore and is also evidence of colder, denser water moving underneath lighter water pushing it upwards in the process. Lastly, a sharp increase in sediment concentrations is recorded by the OBS located at 1 meter above the bottom corresponding to the rotor-like feature at the head of the bore which gives an indication of sediment being resuspended during this time.

The head is then followed by, what will consequently be called the "body" of the bore. Here, the highest acoustic backscatter values (Figure 5.3d) are recorded indicating an elevated concentration of particles in the water. Together with the persistently high flow velocities, predominantly located in the middle of the observed water column between 10 m and 40 m, this also suggests a substantial amount of particle transport. Furthermore, the presence of high-frequency temperature fluctuation near the seabed (Figure 5.3e) suggest increased levels of turbulence near the seabed. The velocity direction during this time remains uniform upcanyon and shows a dominant flow in the alongcanyon direction (Figure 5.2). Suspended particle concentrations measured by the OBS exceed 20 mg/L in this region. However, they seem to be confined to the bottom layer as increased acoustic backscatter values do not extend further than 15 m above the seabed. Overall, the extent of the bottom layer seems to remain relatively unaffected given the sudden hydrodynamic changes occurring as the bore passes and does not increase in extent more than a few meters relative to its conditions beforehand. The profile of the vertical velocities does not show a coherent picture during the passage of the body of the bore but shows some of the largest downward velocities recorded during this event with values up to 2.5 cm/s.

The trailing edge, or "tail" of the bore is characterised by a sharp drop in velocities coinciding with a sudden vertical excursion of sediment into the water column as the flow reverses from the upcanyon to the downcanyon direction. As the bore passes, strong upward velocities are recorded in the upper two thirds of the observed water column exceeding values of 2 cm/s. This corresponds to a sudden increase in sediment concentration and acoustic backscatter with values reaching about half of the maximum values recorded during the body of the bore ($\approx$ 10 mg/L). While consisting of less suspended matter overall, the extent of the particle layer nearly doubles up to heights of 30 m above the seabed in comparison to conditions before or during the passage of the bore.

The period immediately after Bore 1 is characterised by low current velocities in the downcanyon direction and decreasing SPM concentrations suggest settling out of particles. In contrast to other flow reversals recorded at other points during the time series (Figure 5.1), the downcanyon direction is less pronounced with current directions being less homogeneous throughout the water column and vertical velocities rarely exceeding 1 cm/s. Since the suspended matter concentration is shown with a logarithmic scale in Figure 5.3e, the seemingly linear slope corresponds to a logarithmic settling process. The temperature profile remains constant during this time with the absence of high-frequency fluctuations further supporting that calmer conditions are present and turbulence levels have strongly declined.

Conclusively, it should be noted that another internal tidal bore, Bore 2, is observed approximately 6 hours after Bore 1. Its characteristics are similar to that of Bore 1 with a distinct rotor-like structure at its head and a sharp temperature drop as it moves in. However, the overall magnitude of each of these features is significantly smaller and, apart from an uplift of sediment as the even colder water moves underneath the less cold water, no sediment resuspension during the body of the bore is recorded.

5.2 Discussion

The objective of this chapter is to present observations of nonlinear internal wave breaking at the bottom lander at 2500 m water depth and to investigate its influence on sediment resuspension. It was further hypothesised that this internal wave breaking led to the formation of an internal tidal bore that caused the sediment resuspension recorded there.

In the first section, observations of two internal wave regimes were presented where high levels of asymmetry in the length of the up- and downcanyon flow phases suggested nonlinear wave steepening, an important indicator for internal wave breaking (see Section 1.2.3). Additionally, evidence of a bore-like feature occurring on September 14 were presented mainly supported by the distinct vertical velocity profile at its leading edge indicating the presence of a rotor. This was further supported by observations of small scale temperature fluctuations that indicated enhanced levels of turbulence. Evidence for sediment resuspension during this episode was provided by a coherent signal in the optical backscatter recorded by the OBS mounted at 1 mab and acoustic backscatter values recorded by the upward facing ADCP with both showing the highest levels of particle concentrations near the seafloor as the head of the bore passes. After the bore had passed, particles showed an increased vertical extent into the water column and the OBS near the seafloor recorded a logarithmic decline in particle concentrations. Based on this information, we postulate that two different manifestations of internal wave breaking were observed at the bottom lander with each corresponding to one of the two regimes introduced in Section 5.1.1.

The first manifestation is that of an internal wave shoaling with increasing intensity during the yellow periods. This is based on the gradual increases in asymmetry that was found in both the current velocity magnitude and temperature profiles. This asymmetry is interpreted as evidence for the back of the wave catching up to the front of the wave as the troughs slow down due to interactions with the bottom topography. The second manifestation is the subsequent breaking of the wave, corresponding to the transition of the yellow to the red regime, especially from period I to II. This is supported by the shorter asymmetric temperature profile of the third peak compared to the ones before, indicating that the internal wave reached a critical threshold causing it to break rather than to shoal further.

Overall, we postulate that this breaking mechanism follows that of a plunging-collapsing breaker; an intermediate form of the three classes of internal wave breaking introduced in Section 1.2.3, an overview of which is provided in Figure 5.4. We suggest this intermediate
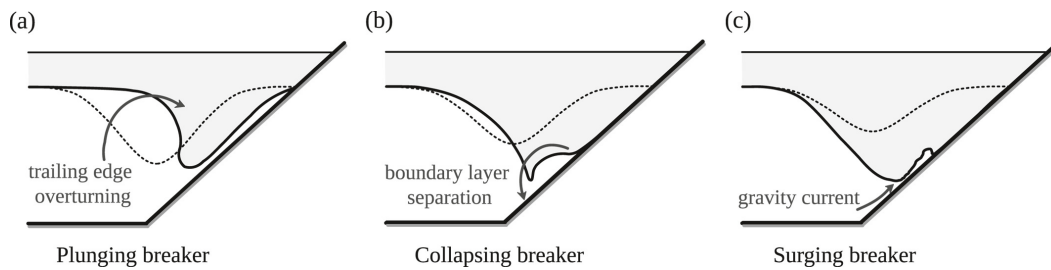
Fig. 5.4: Schematic representation of the three internal wave breaking mechanisms introduced in Section 1.2.3. Arrows show the main instabilities for each breaker type. Dotted lines show the unaltered shape of the incident wave. Taken from La Forgia, Cavaliere, et al. (2021).

form since the observations contain the key characteristics of both breaking mechanisms. The plunging breaker mechanism is characterised by high levels of steepening at the trailing edge of the wave, followed by a strong clockwise overturning circulation. While we do not have evidence of latter, the high levels of asymmetry found during the yellow phase not only indicate high levels of wave steepening but the shape of the temperature profile also indicates that this happens at the trailing edge of the wave. The collapsing breaker mechanism is associated with a fast downward movement in the adverse pressure gradient region of the internal wave causing boundary layer separation and the formation of a gravity current reestablishing hydrodynamic conditions. This not only explains the presence of the internal tidal bore (i.e. the gravity current), but also may explain the absence of a significant backflow during the downcanyon flow phase. Since the dense water would actually be returning to its equilibrium position rather than being displaced, no backflow would occur due to the reestablishment of hydrodynamic conditions. This is further supported by the observation that the bore seems to be a bottom-bound feature, best visualised through its wedge-like shape in Figure 5.3a. Since the gravity current, within the collapsing breaker mechanism, is caused by bottom boundary layer separation, it would also show as a bottom-bound feature. The strong upward velocities and the presence of the rotor can then be interpreted as consequences of the colder, denser water pushing itself underneath the less dense water in front of it.

The only significant sediment response is recorded as the bore passes the bottom lander. The response can be split up into three different aspects with sediment resuspension taking place near its head, sediment transport dominating the body of the bore and settling as well as vertical expansion occurring after its passage. Sediment resuspension during the passage of the head of the bore is supported by the sharp increase in sediment concentrations recorded near the seafloor as the rotor passes. This is further backed up by previous findings in literature where "abrupt bursts of high bed stress associated with a rotor at the leading edge", have been found to be the main cause of resuspension events caused by internal tidal bores (Boegman and Stastna, 2019). Furthermore, Hosegood et al. (2004) and Bonnin et al. (2006) have also found that upslope propagating boluses dominated resuspension events in their observations along the Rockall continental slope.

Significant sediment advection and transport during the passage of the body of the bore is derived from the presence of large current velocity magnitudes and high overall

particle concentrations recorded by the ADCP and distinct, short-lived drops in sediment concentration measured by the OBS close to the seafloor. While it is straightforward that high velocities combined with high concentrations of particles lead to enhanced particle transport, the drops recorded in the OBS give further indication that particles are advected rather than locally resuspended during this time. This conclusion is based on the fact that these drops in sediment concentration occur too quickly to be caused by settling. This suggests that clearer water is rushing past the sensor which is quickly followed by more turbid water. This indicates that the sediment responsible for the increase in turbidity is not being resuspended locally but is instead advected by the high velocities present during the body of the bore.

The last aspect of the sedimentary response consists of the settling of coarser sediment as well as the vertical dispersion of finer sediment higher up into the water column after the bore has passed the bottom lander. The settling of coarser sediment is supported by the logarithmic decline in sediment concentrations recorded by the OBS close to the seafloor. Furthermore, the presence of some of the lowest velocity magnitudes recorded throughout the measurement period suggest low levels of water movement and turbulence, providing favourable conditions for particle settling. This is also supported by numerical simulations run by Cheng et al. (2023) who have found that non-spherical, natural particles show a logarithmic increase in settling velocity in quiescent water. The vertical expansion of particles is observed via increased values of acoustic backscatter in higher regions of the water column by the ADCP. The occurrence of this phenomenon could be connected to an abrupt change in dynamic pressure as current velocities decline rapidly in magnitude over a short period of time once the bore has passed. In general, dynamic pressure describes the pressure exerted by fluid motion and is directly proportional to the square of the velocity magnitude (Kundu, 1990). Consequently, the rapid decline in velocities also causes an abrupt decrease in pressure causing finer sediment particles to be sucked up into the water column. This might also explain the confinement of high particle concentrations to the seafloor during the body of the bore as, conversely, a high dynamic pressure caused by the high current velocities, presses sediment particles towards the seafloor.

While this chapter provides strong evidence of internal wave breaking taking place and the presence of an internal tidal bore able to resuspend sediment, the interpretations drawn from the observations have several important limitations. First, the observations presented in this chapter can only be considered a local snapshot, especially of the internal tidal bore, as these features were only recorded at the bottom lander position. Although their presence was verified by multiple, independent instruments, the spatial evolution of these features before and after they pass the bottom lander is speculative.

Furthermore, the interpretation of local sediment resuspension by the internal tidal bore is qualitatively based on the observations and supporting literature but has not been quantitatively investigated due to time constraints. This means that these results should be verified by calculating the actual bed shear stress exerted by the bore and whether it surpasses the threshold necessary for sediment resuspension under local conditions.

Lastly, the acoustic backscatter values recorded by the ADCP have not been corrected for beam attenuation. Beam attenuation occurs due to the scattering and absorption of sound waves as well as radial spreading of the emitted signal as it travels further away from the

transducer at the head of the instrument. This causes an inherent weakening of the signal with distance, resulting in particle concentrations further away being underestimated in comparison to those recorded close to the instrument's head. Thus, the absolute values recorded by the instrument should be treated with caution. Correcting the signal by accounting for this attenuation might reveal more particle structures higher up in the water column and is necessary if the absolute value of acoustic backscatter is to, for example, be converted to sediment concentration.

Overall, the findings of this chapter have several important implications for understanding sediment transport and internal wave dynamics in Capbreton Canyon. On the one hand, the strong tidally rectified flow in the upcanyon direction, especially during the occurrence of the internal tidal bore, combined with the observed sediment resuspension suggests a potential countermechanism to the downcanyon sediment transport caused by turbidity currents. The presence of internal tidal bores may thus be able to periodically reverse the direction of sediment transport, pushing sediment back up the canyon. This mechanism could be a significant contributor to the long-term geological evolution of the canyon system. On the other hand, the observed uplift of finer sediment into the water column suggests a connection to observations of intermediate nepheloid layers as the sediment might be transported offshore along isopycnals. So far, this vertical expansion is mainly thought to arise from the interactions of successive internal wave breaking events by interactions of a second wave with the run-up of the first wave. This study, however, provides evidence that this vertical expansion of sediment into the water column can also be caused by a single event, in this case postulated to be caused by an abrupt change in dynamic pressure.

Conclusion and Outlook

This study set out to investigate the complex tidal dynamics of Capbreton Canyon and their connection to resuspension of sediment. More specifically, observations obtained at various depths and locations along the canyon's axis were used to gain insights into how internal tides interact with the canyon's topography and influence local sediment dynamics.

The results of this study indicate that internal wave activity is significantly enhanced in regions where the bottom slope of the canyon matches that of the internal wave beams which leads to focusing of internal wave energy and enhanced levels of turbulence near the seafloor. Supporting evidence was provided in the form of observations obtained by ADCPs and an OBS mounted on a bottom lander deployed at a depth of 2500 m on the canyon's thalweg. Here, internal wave breaking and the formation of an internal tidal bore was observed whereas the latter led to significant sediment resuspension as well.

This enhanced internal wave activity likely plays an important role in the mixing processes of the canyon, influencing hydrodynamic conditions locally as well as along the Cantabrian and Aquitaine margins. Additionally, the mixing induced by internal wave breaking suggests that internal waves are a significant contributor to the sediment and nutrient fluxes in the horizontal but also vertical direction, likely influencing biological productivity further up in the water column as well. Furthermore, the sediment resuspension followed by transport in the upcanyon direction, indicates that the observed processes provide a countermechanism to the predominantly downcanyon flux of matter within submarine canyons.

The limitations of this study can mainly be attributed to temporal as well as spatial constraints. First, the observation period did not extend beyond seven or eight days. While it provides enough data to evaluate periodic processes related to the semidiurnal tide, the measurement window is too short to investigate diurnal tidal influences, as well as those caused by seasonal or longer-term atmospheric variations. Therefore, this study cannot account for changes in internal wave activity that arise over longer time periods, which could influence the location and extent of some of the processes observed here such as internal wave breaking or sediment resuspension. Additionally, interpretations were limited by the spatial availability of data. Due to the large distances necessary between measurement locations to cover such a large research area, the measurements obtained at the moorings and the bottom lander provide only snapshots of the local conditions. As a result, most of the observations are not complemented by records at other locations, making it impossible to evaluate the spatial evolution of the observed features. This also makes it difficult to extrapolate the results to the broader canyon system.

Building on the results of this study and its limitations, future research has numerous opportunities to expand the knowledge of Capbreton Canyon and further investigate the processes described in this study.

One opportunity is the deployment of long-term, continuous monitoring at key locations throughout the canyon such as in near-critical regions for the internal semidiurnal tide, e.g. near the bottom lander site. This would provide a clearer picture of how the processes described there evolve over time and under varying tidal, atmospheric and oceanographic conditions. In particular, the influence of seasonal stratification, the presence of a pronounced North-Iberian current or the influence of the highly energetic storm and wave climate of the Bay of Biscay should be investigated as these factors likely contributed to the variability observed in this study.

Due to its close location to the coast and its path running parallel to the northern coast of Spain, Capbreton Canyon also possesses the unique possibility to act as a model system for studying internal wave conditions within a complex submarine canyon. There are several reasons why Capbreton Canyon is particularly suited for this purpose. First, it is located in the Bay of Biscay, one of the most active areas of internal tide generation worldwide (Baines, 1982) which makes internal tides interacting with the canyon more likely to occur. Second, its entire length runs relatively close to the shore, making deployments of instruments easier and more accessible than for other submarine canyons further out at sea. This proximity also allows for the continuous measurement of surface conditions based on land, as is already being done for the shallower regions by, for example, Caballero et al. (2020).

Bibliography

Abadie, S., Butel, R., Mauriet, S., Morichon, D., and Dupuis, H. (2006). „Wave climate and longshore drift on the South Aquitaine coast". In: *Continental Shelf Research* 26.16, pp. 1924–1939. DOI: 10.1016/j.csr.2006.06.005.

Alberty, M. S., Billheimer, S., Hamann, M. M., Ou, C. Y., Tamsitt, V., Lucas, A. J., and Alford, M. H. (2017). „A reflecting, steepening, and breaking internal tide in a submarine canyon". In: *Journal of Geophysical Research: Oceans* 122.8, pp. 6872–6882. DOI: 10.1002/2016JC012583.

Amaro, T., Huvenne, V., Allcock, A. L., Aslam, T., Davies, J. S., Danovaro, R., de Stigter, H. C., Duineveld, G., Gambi, C., Gooday, A. J., Gunton, L. M., Hall, R., Howell, K. L., Ingels, J., Kiriakoulakis, K., Kershaw, C. E., Lavaleye, M., Robert, K., Stewart, H., van Rooij, D., White, M., and Wilson, A. M. (2016). „The Whittard Canyon – A case study of submarine canyon processes". In: *Progress in Oceanography* 146, pp. 38–57. DOI: 10.1016/j.pocean.2016.06.003.

Arai, K., Naruse, H., Miura, R., Kawamura, K., Hino, R., Ito, Y., Inazu, D., Yokokawa, M., Izumi, N., Murayama, M., and Kasaya, T. (2013). „Tsunami-generated turbidity current of the 2011 Tohoku-Oki earthquake". In: *Geology* 41.11, pp. 1195–1198. DOI: 10.1130/G34777.1.

Aslam, T., Hall, R. A., and Dye, S. R. (2018). „Internal tides in a dendritic submarine canyon". In: *Progress in Oceanography* 169, pp. 20–32. DOI: 10.1016/j.pocean.2017.10.005.

Augris, C. (1993). *PLABAS cruise,Thalia R/V*. DOI: 10.17600/93000660.

Augris, C. (1994). *PLABAS 94/2 cruise,Thalia R/V*. DOI: 10.17600/94070180.

Augris, C. and Lericolais, G. (1995). *PLACETA / PLABAS 3 cruise,Thalia R/V*. DOI: 10.17600/95070070.

Baines, P. G. (1982). „On internal tide generation models". In: *Deep Sea Research Part A. Oceanographic Research Papers* 29.3, pp. 307–338. DOI: 10.1016/0198-0149(82)90098-X.

Baker, M. L., Hage, S., Talling, P. J., Acikalin, S., Hilton, R. G., Haghipour, N., Ruffell, S. C., Pope, E. L., Jacinto, R. S., Clare, M. A., and Sahin, S. (2024). „Globally significant mass of terrestrial organic carbon efficiently transported by canyon-flushing turbidity currents". In: *Geology* 52.8, pp. 631–636. DOI: 10.1130/G51976.1.

Barbot, S., Lyard, F., Tchilibou, M., and Carrere, L. (2021). „Background stratification impacts on internal tide generation and abyssal propagation in the western equatorial Atlantic and the Bay of Biscay". In: *Ocean Science* 17.6, pp. 1563–1583. DOI: 10.5194/os-17-1563-2021.

Baringer, M. O. and Price, J. F. (1997). „Mixing and Spreading of the Mediterranean Out-flow". In: *Journal of Physical Oceanography* 27.8, pp. 1654–1677. DOI: 10.1175/1520-0485(1997)027{\textless}1654:MASOTM{\textgreater}2.0.CO;2.

Bode, A., Varela, M., Casas, B., and González, N. (2002). „Intrusions of eastern North Atlantic central waters and phytoplankton in the north and northwestern Iberian shelf during spring". In: *Journal of Marine Systems* 36.3-4, pp. 197–218. DOI: 10.1016/S0924-7963(02)00187-2.

Boegman, L., Ivey, G. N., and Imberger, J. (2005). „The degeneration of internal waves in lakes with sloping topography". In: *Limnology and Oceanography* 50.5, pp. 1620–1637. DOI: 10.4319/lo.2005.50.5.1620.

Boegman, L. and Stastna, M. (2019). „Sediment Resuspension and Transport by Internal Solitary Waves". In: *Annual Review of Fluid Mechanics* 51.1, pp. 129–154. DOI: 10.1146/annurev-fluid-122316-045049.

Bonnin, J., van Haren, H., Hosegood, P., and Brummer, G.-J. A. (2006). „Burst resuspension of seabed material at the foot of the continental slope in the Rockall Channel". In: *Marine Geology* 226.3-4, pp. 167–184. DOI: 10.1016/j.margeo.2005.11.006.

Bourillet, J.-F., Zaragosi, S., and Mulder, T. (2006). „The French Atlantic margin and deep-sea submarine systems". In: *Geo-Marine Letters* 26.6, pp. 311–315. DOI: 10.1007/s00367-006-0042-2.

Brocheray, S., Cremer, M., Zaragosi, S., Schmidt, S., Eynaud, F., Rossignol, L., and Gillet, H. (2014). „2000years of frequent turbidite activity in the Capbreton Canyon (Bay of Biscay)". In: *Marine Geology* 347, pp. 136–152. DOI: 10.1016/j.margeo.2013.11.009.

Caballero, A., Mulet, S., Ayoub, N., Manso-Narvarte, I., Davila, X., Boone, C., Toublanc, F., and Rubio, A. (2020). „Integration of HF Radar Observations for an Enhanced Coastal Mean Dynamic Topography". In: *Frontiers in Marine Science* 7, p. 588713. DOI: 10.3389/fmars.2020.588713.

Cacchione, D. A., Pratson, L. F., and Ogston, A. S. (2002). „The shaping of continental slopes by internal tides". In: *Science (New York, N.Y.)* 296.5568, pp. 724–727. DOI: 10.1126/science.1069803.

Cheng, X., Cao, Z., Li, J., and Borthwick, A. (2023). „A numerical study of the settling of non-spherical particles in quiescent water". In: *Physics of Fluids* 35.9. DOI: 10.1063/5.0165555.

Cirac, P. (1998). *ITSAS*. DOI: 10.18142/266.

Cirac, P. (2001). *ITSAS II cruise,Le Suroît R/V*. DOI: 10.17600/1020050.

Cirac, P. (2002). *ITSAS VI cruise,Thalia R/V*. DOI: 10.17600/2070100.

Cirac, P. (2004). *PROSECAN 2 cruise,Thalia R/V*. DOI: 10.17600/4070150.

Cirac, P., Bourillet, J.-F., Griboulard, R., and Normand, A. (2001). „Le canyon de Capbreton : nouvelles approches morphostructurales et morphosédimentaires. Premiers résultats de la campagne Itsas". In: *Comptes Rendus de l'Académie des Sciences - Series IIA - Earth and Planetary Science* 332.7, pp. 447–455. DOI: 10.1016/S1251-8050(01)01557-9.

Codiga, D. L. (2011). *Unified tidal analysis and prediction using the UTide Matlab functions*. DOI: 10.13140/RG.2.1.3761.2008.

CREMER Michel (2010). *SARGASS cruise,Pourquoi pas ? R/V*. DOI: 10.17600/10030080.

Daubechies, I. (1990). „The wavelet transform, time-frequency localization and signal analysis“. In: *IEEE Transactions on Information Theory* 36.5, pp. 961–1005. DOI: `10.1109/18.57199`.

Dauhajre, D. P., McWilliams, J. C., and Hypolite, D. (2023). „Interactions Between Internal Tidal Bores and Submesoscale Currents on the Continental Shelf“. In: *Journal of Geophysical Research: Oceans* 128.2, e2022JC018747. DOI: `10.1029/2022JC018747`.

de Stigter, H. C., Jesus, C. C., Boer, W., Richter, T. O., Costa, A., and van Weering, T. C. (2011). „Recent sediment transport and deposition in the Lisbon–Setúbal and Cascais submarine canyons, Portuguese continental margin“. In: *Deep Sea Research Part II: Topical Studies in Oceanography* 58.23-24, pp. 2321–2344. DOI: `10.1016/j.dsr2.2011.04.001`.

Deregnaucourt, D. and Boillot, G. (1982). *New structural map of the Bay of Biscay*.

Downing, J. (2006). „Twenty-five years with OBS sensors: The good, the bad, and the ugly“. In: *Continental Shelf Research* 26.17-18, pp. 2299–2318. DOI: `10.1016/j.csr.2006.07.018`.

Farge, M. (1992). „Wavelet Transforms And Their Applications To Turbulence“. In: *Annual Review of Fluid Mechanics* 24.1, pp. 395–457. DOI: `10.1146/annurev.fluid.24.1.395`.

Ferrer, O., Roca, E., Benjumea, B., Muñoz, J. A., Ellouz, N., and Team, M. (2008). „The deep seismic reflection MARCONI-3 profile: Role of extensional Mesozoic structure during the Pyrenean contractional deformation at the eastern part of the Bay of Biscay“. In: *Marine and Petroleum Geology* 25.8, pp. 714–730. DOI: `10.1016/j.marpetgeo.2008.06.002`.

Fraga, F., Mouriño, C., and Manríquez, M. (1982). „Las masas de agua en la costa de Galicia: junio-octubre“. In: *0020-9953*.

Garrett, C. (2003). „Ocean science. Enhanced: internal tides and ocean mixing“. In: *Science (New York, N.Y.)* 301.5641, pp. 1858–1859. DOI: `10.1126/science.1090002`.

Gaudin, M., Mulder, T., Cirac, P., Berné, S., and Imbert, P. (2006). „Past and present sedimentary activity in the Capbreton Canyon, southern Bay of Biscay“. In: *Geo-Marine Letters* 26.6, pp. 331–345. DOI: `10.1007/s00367-006-0043-1`.

GEBCO Compilation Group (2024). *GEBCO 2024 Grid*.

Gerkema, T. and Zimmerman, J. (2008). *An introduction to internal waves*.

Gillard, B., Harbour, R. P., Nowald, N., Thomsen, L., and Iversen, M. H. (2022). „Vertical Distribution of Particulate Matter in the Clarion Clipperton Zone (German Sector)—Potential Impacts From Deep-Sea Mining Discharge in the Water Column“. In: *Frontiers in Marine Science* 9. DOI: `10.3389/fmars.2022.820947`.

Gómez-Ballesteros, M., Arrese, B., Díez, I. P., Galparsoro, I., Sánchez-Guillamón, O., Martínez-Carreño, N., Sayago, M., López-Rodríguez, C., Rodríguez, A., and Sánchez, F. (2022). „Morphosedimentary characterization of the Capbreton submarine canyon system, Bay of Biscay (Cantabrian Sea)“. In: *Estuarine, Coastal and Shelf Science* 274, p. 107955. DOI: `10.1016/j.ecss.2022.107955`.

Greene, H. G., Maher, N. M., and Paull, C. K. (2002). „Physiography of the Monterey Bay National Marine Sanctuary and implications about continental margin development“. In: *Marine Geology* 181.1-3, pp. 55–82. DOI: `10.1016/S0025-3227(01)00261-4`.

Guiastrennec-Faugas, L., Gillet, H., Silva Jacinto, R., Dennielou, B., Hanquiez, V., Schmidt, S., Simplet, L., and Rousset, A. (2020). „Upstream migrating knickpoints and related sedimentary processes in a submarine canyon from a rare 20-year morphobathymetric time-lapse (Capbreton submarine canyon, Bay of Biscay, France)". In: *Marine Geology* 423, p. 106143. DOI: 10.1016/j.margeo.2020.106143.

Hall, R. A., Aslam, T., and Huvenne, V. A. (2017). „Partly standing internal tides in a dendritic submarine canyon observed by an ocean glider". In: *Deep Sea Research Part I: Oceanographic Research Papers* 126, pp. 73–84. DOI: 10.1016/j.dsr.2017.05.015.

Harris, P. T., Macmillan-Lawler, M., Rupp, J., and Baker, E. K. (2014). „Geomorphology of the oceans". In: *Marine Geology* 352, pp. 4–24. DOI: 10.1016/j.margeo.2014.01.011.

Harris, P. T. and Whiteway, T. (2011). „Global distribution of large submarine canyons: Geomorphic differences between active and passive continental margins". In: *Marine Geology* 285.1-4, pp. 69–86. DOI: 10.1016/j.margeo.2011.05.008.

Harvey, J. (1982). „j-S relationships and water masses in the eastern North Atlantic". In: *Deep Sea Research Part A. Oceanographic Research Papers* 29.8, pp. 1021–1033. DOI: 10.1016/0198-0149(82)90025-5.

Hosegood, P., Bonnin, J., and van Haren, H. (2004). „Solibore–induced sediment resuspension in the Faeroe–Shetland Channel". In: *Geophysical Research Letters* 31.9. DOI: 10.1029/2004GL019544.

Idier, D., Castelle, B., Charles, E., and Mallet, C. (2013). „Longshore sediment flux hindcast: spatio-temporal variability along the SW Atlantic coast of France". In: *Journal of Coastal Research* 165, pp. 1785–1790. DOI: 10.2112/SI65-302.1.

Intergovernmental Oceanographic Commission, Scientific Committee on Oceanic Research, and International Association for the Physical Sciences of the Ocean (2010). *The International thermodynamic equation of seawater, 2010: calculation and use of thermodynamic properties*. <bound method Organization.get_name_with_acronym of <Organization: United Nations Educational, Scientific and Cultural Organisation.

Jorda, G., Flexas, M. M., Espino, M., and Calafat, A. (2013). „Deep flow variability in a deeply incised Mediterranean submarine valley (Blanes canyon)". In: *Progress in Oceanography* 118, pp. 47–60. DOI: 10.1016/j.pocean.2013.07.024.

Karagiorgos, J., Vervatis, V., and Sofianos, S. (2020). „The Impact of Tides on the Bay of Biscay Dynamics". In: *Journal of Marine Science and Engineering* 8.8, p. 617. DOI: 10.3390/jmse8080617.

Klingebiel, A. and Legigan, P. (1978). „Histoire géologique des divagations de l'Adour". In: *Proc Congr IVème Centenaire du Détournement de l'Adour*, pp. 1578–1978.

Korteweg, D. J. and de Vries, G. (1895). „XLI. On the change of form of long waves advancing in a rectangular canal, and on a new type of long stationary waves". In: *The London, Edinburgh, and Dublin Philosophical Magazine and Journal of Science* 39.240, pp. 422–443. DOI: 10.1080/14786449508620739.

Krieger, S. and Freij, N. (2023). *PyCWT: wavelet spectral analysis in Python*.

Kundu, P. K. (1990). *Fluid mechanics*. Online-ausg. San Diego: Academic Press.

La Forgia, G., Adduce, C., and Falcini, F. (2018). „Laboratory investigation on internal solitary waves interacting with a uniform slope". In: *Advances in Water Resources* 120, pp. 4–18. DOI: 10.1016/j.advwatres.2017.07.027.

La Forgia, G., Cavaliere, D., Adduce, C., and Falcini, F. (2021). „Mixing Efficiency for Breaking Internal Solitary Waves". In: *Journal of Geophysical Research: Oceans* 126.6, e2021JC017275. DOI: 10.1029/2021JC017275.

La Forgia, G., Tokyay, T., Adduce, C., and Constantinescu, G. (2020). „Bed shear stress and sediment entrainment potential for breaking of internal solitary waves". In: *Advances in Water Resources* 135, p. 103475. DOI: 10.1016/j.advwatres.2019.103475.

Le Cann, B. (1990). „Barotropic tidal dynamics of the Bay of Biscay shelf: observations, numerical modelling and physical interpretation". In: *Continental Shelf Research* 10.8, pp. 723–758. DOI: 10.1016/0278-4343(90)90008-A.

Li, M. Z., Prescott, R. H., and Robertson, A. G. (2019). „Observation of internal tides and sediment transport processes at the head of Logan Canyon on central Scotian Slope, eastern Canada". In: *Journal of Marine Systems* 193, pp. 103–125. DOI: 10.1016/j.jmarsys.2019.02.007.

Maas, L. (2019). *Wave Attractors*. Utrecht.

Marques, O. B., Alford, M. H., Pinkel, R., Mackinnon, J. A., Klymak, J. M., Nash, J. D., Waterhouse, A. F., Kelly, S. M., Simmons, H. L., and Braznikov, D. (2021). „Internal Tide Structure and Temporal Variability on the Reflective Continental Slope of Southeastern Tasmania". In: *Journal of Physical Oceanography* 51.2, pp. 611–631. DOI: 10.1175/JPO-D-20-0044.1.

Mashayek, A., Ferrari, R., Merrifield, S., Ledwell, J. R., St Laurent, L., and Garabato, A. N. (2017). „Topographic enhancement of vertical turbulent mixing in the Southern Ocean". In: *Nature Communications* 8.1, p. 14197. DOI: 10.1038/ncomms14197.

Masunaga, E., Arthur, R. S., Fringer, O. B., and Yamazaki, H. (2017). „Sediment resuspension and the generation of intermediate nepheloid layers by shoaling internal bores". In: *Journal of Marine Systems* 170, pp. 31–41. DOI: 10.1016/j.jmarsys.2017.01.017.

Mazières, A., Gillet, H., Castelle, B., Mulder, T., Guyot, C., Garlan, T., and Mallet, C. (2014). „High-resolution morphobathymetric analysis and evolution of Capbreton submarine canyon head (Southeast Bay of Biscay—French Atlantic Coast) over the last decade using descriptive and numerical modeling". In: *Marine Geology* 351, pp. 1–12. DOI: 10.1016/j.margeo.2014.03.001.

Mulder, T., Zaragosi, S., Garlan, T., Mavel, J., Cremer, M., Sottolichio, A., Sénéchal, N., and Schmidt, S. (2012). „Present deep-submarine canyons activity in the Bay of Biscay (NE Atlantic)". In: *Marine Geology* 295-298, pp. 113–127. DOI: 10.1016/j.margeo.2011.12.005.

Normandeau, A., Bourgault, D., Neumeier, U., Lajeunesse, P., St–Onge, G., Gostiaux, L., and Chavanne, C. (2020). „Storm–induced turbidity currents on a sediment–starved shelf: Insight from direct monitoring and repeat seabed mapping of upslope migrating bedforms". In: *Sedimentology* 67.2, pp. 1045–1068. DOI: 10.1111/sed.12673.

Nortek Manuals (2017). *The Comprehensive Manual: AWAC | Aquadopp | Aquadopp Profiler | 2D Horizontal Profiler | Vector | Vectrino*.

Payo-Payo, M., Jacinto, R. S., Lastras, G., Rabineau, M., Puig, P., Martín, J., Canals, M., and Sultan, N. (2017). „Numerical modeling of bottom trawling-induced sediment transport and accumulation in La Fonera submarine canyon, northwestern Mediterranean Sea". In: *Marine Geology* 386, pp. 107–125. DOI: 10.1016/j.margeo.2017.02.015.

Petus, C., Chust, G., Gohin, F., Doxaran, D., Froidefond, J.-M., and Sagarminaga, Y. (2010). „Estimating turbidity and total suspended matter in the Adour River plume (South Bay of Biscay) using MODIS 250-m imagery“. In: *Continental Shelf Research* 30.5, pp. 379–392. DOI: 10.1016/j.csr.2009.12.007.

Pingree, R. and Le Cann, B. (1992). „Three anticyclonic slope water oceanic eDDIES (SWODDIES) in the Southern Bay of Biscay in 1990“. In: *Deep Sea Research Part A. Oceanographic Research Papers* 39.7-8, pp. 1147–1175. DOI: 10.1016/0198-0149(92)90062-X.

Puig, P., Palanques, A., Guillén, J., and El Khatab, M. (2004). „Role of internal waves in the generation of nepheloid layers on the northwestern Alboran slope: Implications for continental margin shaping“. In: *Journal of Geophysical Research* 109.C9. DOI: 10.1029/2004JC002394.

Rainville, L., Johnston, T. M. S., Carter, G. S., Merrifield, M. A., Pinkel, R., Worcester, P. F., and Dushaw, B. D. (2010). „Interference Pattern and Propagation of the M2 Internal Tide South of the Hawaiian Ridge“. In: *Journal of Physical Oceanography* 40.2, pp. 311–325. DOI: 10.1175/2009JPO4256.1.

Rijkenberg, M. J., Baar, H. J. de, Bakker, K., Gerringa, L. J., Keijzer, E., Laan, M., Laan, P., Middag, R., Ober, S., van Ooijen, J., Ossebaar, S., van Weerlee, E. M., and Smit, M. G. (2015). „"PRISTINE", a new high volume sampler for ultraclean sampling of trace metals and isotopes“. In: *Marine Chemistry* 177, pp. 501–509. DOI: 10.1016/j.marchem.2015.07.001.

Ross, L., Pérez-Santos, I., Valle-Levinson, A., and Schneider, W. (2014). „Semidiurnal internal tides in a Patagonian fjord“. In: *Progress in Oceanography* 129, pp. 19–34. DOI: 10.1016/j.pocean.2014.03.006.

Seabold, S. and Perktold, J. (2010). „Statsmodels: Econometric and Statistical Modeling with Python“. In: *Proceedings of the Python in Science Conference*. SciPy. DOI: 10.25080/majora-92bf1922-011.

Shepard, F. P. and Emery, K. O. (1973). „Congo Submarine Canyon and Fan Valley“. In: *AAPG Bulletin* 57.9, pp. 1679–1691.

Swart, N. C., Allen, S. E., and Greenan, B. J. W. (2011). „Resonant amplification of subinertial tides in a submarine canyon“. In: *Journal of Geophysical Research* 116.C9. DOI: 10.1029/2011JC006990.

Tarrés, M., Cerdà-Domènech, M., Pedrosa-Pàmies, R., Baza-Varas, A., Calafat, A., Sanchez-Vidal, A., and Canals, M. (2023). „Transport and distributions of naturally and anthropogenically sourced trace metals and arsenic in submarine canyons“. In: *Progress in Oceanography* 218, p. 103122. DOI: 10.1016/j.pocean.2023.103122.

Thomson, R. E. and Emery, W. J. (2014). *Data analysis methods in physical oceanography*. Elsevier.

Tian, Z., Liu, Y., Zhang, X., Zhang, Y., and Zhang, M. (2022). „Formation Mechanisms and Characteristics of the Marine Nepheloid Layer: A Review“. In: *Water* 14.5, p. 678. DOI: 10.3390/w14050678.

Torrence, C. and Compo, G. P. (1998). „A Practical Guide to Wavelet Analysis“. In: *Bulletin of the American Meteorological Society* 79.1, pp. 61–78. DOI: 10.1175/1520-0477(1998)079{\textless}0061:APGTWA{\textgreater}2.0.CO;2.

Tubau, X., Canals, M., Lastras, G., Rayo, X., Rivera, J., and Amblas, D. (2015). „Marine litter on the floor of deep submarine canyons of the Northwestern Mediterranean Sea: The role of hydrodynamic processes". In: *Progress in Oceanography* 134, pp. 379–403. DOI: 10.1016/j.pocean.2015.03.013.

van Aken, H. M. (2000). „The hydrography of the mid-latitude northeast Atlantic Ocean". In: *Deep Sea Research Part I: Oceanographic Research Papers* 47.5, pp. 757–788. DOI: 10.1016/S0967-0637(99)00092-8.

van Haren, H. (2023). „Detailing secondary frontal bore of internal tides breaking above deep-ocean topography". In: *Journal of Oceanography* 79.6, pp. 581–592. DOI: 10.1007/s10872-023-00699-0.

van Weering, T. C., Koster, B., van Heerwaarden, J., Thomsen, L., and Viergutz, T. (2000). „New technique for long term deep seabed studies". In: *Sea Technology* 2, pp. 17–25.

Vic, C., Naveira Garabato, A. C., Green, J. A. M., Waterhouse, A. F., Zhao, Z., Melet, A., Lavergne, C. de, Buijsman, M. C., and Stephenson, G. R. (2019). „Deep-ocean mixing driven by small-scale internal tides". In: *Nature Communications* 10.1, p. 2099. DOI: 10.1038/s41467-019-10149-5.

Virtanen, P., Gommers, R., Oliphant, T. E., Haberland, M., Reddy, T., Cournapeau, D., Burovski, E., Peterson, P., Weckesser, W., Bright, J., van der Walt, S. J., Brett, M., Wilson, J., Millman, K. J., Mayorov, N., Nelson, A. R. J., Jones, E., Kern, R., Larson, E., Carey, C. J., Polat, İ., Feng, Y., Moore, E. W., VanderPlas, J., Laxalde, D., Perktold, J., Cimrman, R., Henriksen, I., Quintero, E. A., Harris, C. R., Archibald, A. M., Ribeiro, A. H., Pedregosa, F., and van Mulbregt, P. (2020). „SciPy 1.0: fundamental algorithms for scientific computing in Python". In: *Nature Methods* 17.3, pp. 261–272. DOI: 10.1038/s41592-019-0686-2.

Vlasenko, V., Stashchuk, N., Inall, M. E., Porter, M., and Aleynik, D. (2016). „Focusing of baroclinic tidal energy in a canyon". In: *Journal of Geophysical Research: Oceans* 121.4, pp. 2824–2840. DOI: 10.1002/2015JC011314.

Woodson, C. B. (2018). „The Fate and Impact of Internal Waves in Nearshore Ecosystems". In: *Annual review of marine science* 10.Volume 10, 2018, pp. 421–441. DOI: 10.1146/annurev-marine-121916-063619.

Wunsch, C. (1975). „Internal tides in the ocean". In: *Reviews of Geophysics* 13.1, pp. 167–182. DOI: 10.1029/RG013i001p00167.